Design of Wireless Fronthaul With mmWave LOS-MIMO and Sample-Level Coding for O-RAN and Beyond 5G Systems

JUERGEN CEZANNE (Senior Member, IEEE), MEILONG JIANG (Senior Member, IEEE),
ORI SHENTAL (Senior Member, IEEE), AHMED M. BEDEWY, ASHWIN SAMPATH (Senior Member, IEEE),
OZGE KOYMEN (Member, IEEE), AND JUNYI LI (Fellow, IEEE)

Wireless Research & Development Department, Qualcomm Technologies, Inc., Bridgewater, NJ 08807, USA

CORRESPONDING AUTHORS: J. CEZANNE AND M. JIANG (e-mail: jcezanne@qti.qualcomm.com; meiljian@qti.qualcomm.com)

ABSTRACT This paper proposes novel designs of line-of-sight multiple-input multiple-output (LOS-MIMO) and a unique sample-level coding scheme for wireless fronthaul (WFH) deployment in Open Radio Access Network (O-RAN) and beyond the fifth-generation (5G) systems. The objective of these designs is to achieve high capacity, robustness, and ultra-reliability in WFH, providing performance comparable to fiber-optic fronthaul solutions. Firstly, by optimizing array configuration parameters, such as array aperture size, antenna separation, and the proposed analog multipath beamforming scheme, LOS-MIMO operating at millimeter-wave (mmWave) bands emerges as a critical enabler for WFH, delivering the required high data rates to support lower-level split options as defined by the 3rd Generation Partnership Project for fronthaul networks. Furthermore, the use of a non-uniform array design effectively enhances the robustness of WFH by addressing the performance degradation caused by spatial aliasing when LOS-MIMO is employed with uniformly spaced linear array at shorter distances. Additionally, the proposed augmented sample-level coding not only seamlessly integrates with the fronthaul design but also provides benefits for ultra-reliable applications carried over the fronthaul. Through extensive simulations at both system and link levels, it is demonstrated that employing high-rank LOS-MIMO at mmWave bands for WFH ensures high capacity, robustness, and reliable performance. Overall, the analysis presented in this paper establishes that WFH can be effectively designed to meet the stringent requirements of fronthaul networks and represents an attractive option for future disaggregated RAN deployments.

INDEX TERMS Wireless fronthaul, LOS-MIMO, sample-level coding, mmWave, open RAN, disaggregated RAN, Beyond 5G.

I. INTRODUCTION

WIRELESS networks have been evolving at a frenetic pace to meet the ever-increasing demands for higher capacity, lower latency, and massive number of connections. In the fifth generation (5G) radio access networks (RAN), millimeter-wave (mmWave) and higher band radios are instrumental in achieving such stringent requirements. The network deployment must go through significant densification to meet the extremely high demand of data traffic [1]. This imposes various challenges to the network architecture as well as to the design of fronthaul (FH) transport links in the network.

5G systems introduce significant architectural flexibility by disaggregating the classic base station into three logical nodes: the central unit (CU), the distributed unit (DU), and the radio unit (RU). Fronthaul refers to the connection links between DUs and RUs, while backhaul pertains to the connections between CUs and the core network. Conventionally, fiber-based connections have been the mainstream technology for fronthaul. However, there are several motivations for considering wireless fronthaul (WFH) as an alternative.

- Cost-Effectiveness: Wireless fronthaul offers potential cost savings compared to laying physical fiber,

especially in areas where it is difficult or expensive to deploy fiber cables. This is particularly important when expanding network coverage to rural or remote areas.

- Scalability and Density: With the advent of 5G and beyond, networks must support a growing number of devices and higher data rates. Wireless fronthaul is better equipped to scale and support denser small cell deployments, accommodating the increasing demands of connected devices and applications.
- Dynamic Network Configuration: Wireless fronthaul enables dynamic reconfiguration and optimization of the network. Operators can easily adjust the placement of DUs and RUs to optimize network performance and resource utilization, providing greater adaptability to changing conditions.
- Flexibility and Rapid Deployment: Compared to laying wired fronthaul infrastructure, wireless fronthaul offers more flexibility and quicker deployment options, reducing both time and costs associated with installing fiber cables.

In the existing literature, there have been efforts to explore the application of wireless technology to fronthaul transport. In [2], a high-level overview of 5G fronthaul and backhaul wireless transport based on mmWave technology is provided, including data rate and latency requirements for three emerging fronthaul interfaces with each corresponding to one functional split option. Reference [3] explores mmWave fronthauling with flexible reconfigured RU states and movable DU placements. The investigation briefly considers channel capacity based on received power, path loss, separation distances between DUs and RUs, and different mmWave bands. However, these above references do not clearly address how to meet the capacity requirements in fronthaul transport links and tackle the challenges specific to wireless fronthaul. Moreover, fronthaul transport links typically have much higher data rate and latency requirements compared to backhaul transport links, which means wireless backhaul solutions introduced in [4], [5] may not directly apply to wireless fronthaul. In [6], an overview of emerging fronthaul interfaces and requirements is discussed, along with a few enabling technologies and solutions that can be applied in WFH to meet the capacity and latency requirements for future fronthaul networks. The technologies mentioned, such as fronthaul compression, leveraging new higher band spectrum, optimizing high rank line-of-sight multiple-input multiple-output (LOS-MIMO), and utilizing reconfigurable intelligent surfaces (RIS), are only discussed at a high-level.

This paper proposes enhanced designs of mmWave LOS-MIMO for wireless fronthaul in order to address the high capacity and ultra-reliability requirements of fronthaul transport links. The main contributions of the paper are as follows:

- Theoretical analysis: A systematic theoretical analysis is presented to determine the achievable degrees of freedom (DoF) in LOS-MIMO systems. The DoF is shown to depend on various factors, including the aperture size of the transmitter (Tx) and receiver (Rx), the distance between them, the orientation of the antenna arrays, the wavelength, and the antenna separation. The analysis also delves into the effects of space discretization, array aperture size, and transmission distance on the achievable DoF, while studying the impact of array misalignment on system robustness.
- Enhanced designs: The paper proposes different designs tailored for the fronthaul use case, considering a wide range of distances. Enhanced techniques are suggested to improve LOS-MIMO performance, including a non-uniform array design to mitigate performance dips caused by spatial aliasing with uniform linear arrays (ULA) at shorter distances. Additionally, a multipath analog beamforming scheme is proposed, which exploits more than one spatial direction simultaneously in addition to the LOS direction, achieved through a hybrid-connected array architecture.
- Outer code scheme: A sample-level outer code scheme is proposed that aligns very well with the inherent sample-level operation of the fronthaul. In contrast to the commonly-used bit-level coding, the proposed scheme *directly* encodes the fronthaul quantized data symbols, through a Discrete Fourier Transform (DFT)-based processing. It then appends the newly-generated redundancy samples to the original data symbol block. Adopting a sample-wise, rather than bit-wise, coding mechanism assists in overcoming residual errors that may remain after utilizing a conventional (bit-level) inner code. Hence, introducing such a sample-level outer code facilitates meeting the stringent reliability requirements of the wireless fronthaul links.

The paper is organized as follows: Section II provides a brief introduction to Open Radio Access Network (O-RAN) and disaggregated RAN architecture, along with the fronthaul transport requirements for the specific use case scenario under study. Section III begins with a theoretical analysis of the available DoF in LOS-MIMO systems, considering both continuous aperture and discretized antenna arrays (relevant to practical phased arrays). It then delves into the proposed tailored designs for wireless fronthaul, including optimization of array configuration (e.g., aperture size and antenna separation) based on the desired DoF, non-uniform array design, and multipath analog beamforming techniques. Section IV focuses on the outer code scheme aimed at enhancing fronthaul link reliability. This scheme complements the conventional inner code used and helps overcome residual errors, thereby meeting the stringent reliability requirements of wireless fronthaul links. Finally, Section V concludes the paper, summarizing its main contributions and discussing potential future research directions.

II. DISAGGREGATED RAN ARCHITECTURE AND REQUIREMENTS FOR FRONTHAUL

As the RAN architecture evolves, the 3rd Generation Partnership Project (3GPP) has defined eight functional split options (SO) in [7], namely SO 1 to SO 8, targeting to answer how to split RAN functions, where to place those functions, and what transport is required to interconnect them. Higher number of split options shift more complexity to the central unit, allowing better coordination across sectors and cells. However, this comes with increased capacity and latency requirements for the fronthaul.

The O-RAN Alliance is committed to reshape the RAN industry by promoting intelligent, open, virtualized and inter-operable mobile networks. O-RAN defines standards in three areas: RAN disaggregation, RAN automation, and RAN virtualization [8]. O-RAN specifications complement those of 3GPP by introducing interface profiles, new open interfaces, and new nodes. Like 3GPP, O-RAN splits the base station into three different components: O-RU (O-RAN Radio Unit), O-DU (O-RAN Distributed Unit) and O-CU (O-RAN Central Unit). Specifically, O-RAN introduces the open fronthaul interface (O-FH) between O-DU and O-RU, categorized as SO 7-2x [8]. In this paper, we will focus on studying the feasibility of supporting SO 7 through WFH. Supporting other widely adopted SOs through wireless transport, such as SO 2 and SO 6, is also feasible due to lower capacity and latency requirements compared to SO 7.

In the studied deployment use case (as shown in Fig. 1), the O-CU and O-DU are co-located at the central office, while the O-RUs are located at remote sites. The O-RUs serve end users with access links (Uu interface) either through sub-6 GHz bands (FR1) or mmWave bands (FR2) as defined by 3GPP. Based on SO 7-2x, the O-DU handles high physical layer (PHY) and above functions, while the O-RU performs low-PHY and radio frequency (RF) functions.

Rather than using fiber, the paper proposes employing a mmWave E-band based LOS-MIMO link, operating at an 80 GHz carrier frequency, as the physical medium for fronthaul transport. To achieve this, WFH modules are introduced at both the O-DU and O-RU ends. These WFH modules can be integrated into the O-DU and O-RU units or designed as plug-and-play modules interconnected with Ethernet cables. As illustrated in Fig. 1, one example shows a WFH module at the O-DU connected to a time-sensitive network (TSN) switch, while another WFH module at the O-RU is connected to an O-RU unit via Ethernet cables. Wireless fronthauling offers the advantage of flexible point-to-multipoint wireless links, allowing a single O-DU to be connected to multiple O-RUs. In addition, the O-RUs can be placed at a wide range of distances and locations, targeting the areas where fiber connections are presumably not feasible.

Despite its advantages in flexible, scalable, and low-cost deployment [9], WFH faces various challenges in meeting the stringent requirements of 5G and beyond systems in guaranteeing high data rate, low latency, supporting point-to-multipoint deployment, and so on. The required data
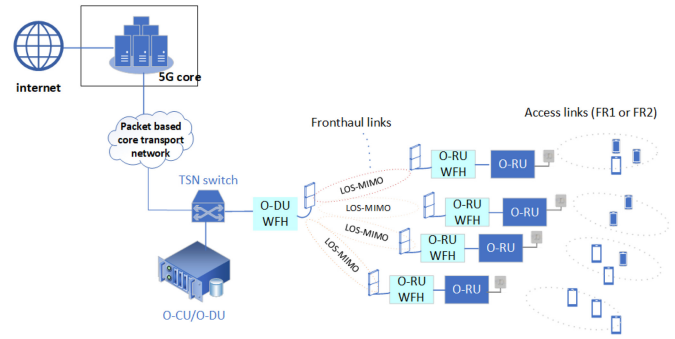

FIGURE 1. Exemplary deployment use-case for wireless fronthaul.

rate at fronthaul link could be exceptionally high for certain split options like SO 7 and SO 8 [6], [7], since it requires the transfer of complex-valued samples carrying in-phase and quadrature (I/Q) components. Table 1 presents the required fronthaul date rate for a specific deployment use case depicted in Fig. 1. The table includes typical operating parameters for FR1 and FR2 deployed in access networks (Uu) in the first three columns. The middle two columns outline the assumed operating parameters for the wireless FH links, which will be utilized for evaluating the performance of LOS-MIMO FH links in subsequent sections. The last two columns show the required FH data rate to fully support the access (Uu) links in FR1 and FR2, taking into account access link parameters defined in the table. Specifically, the required FH data rate can be determined as [7], [10]

$$C_{FH} = \frac{N_{layer} \times N_{tones} \times N_{IQbits}}{\tau_{sym} \times (1 + CP_{oh}) \times (1 + FH_{oh})}, \qquad (1)$$

where N_{layer}, N_{tones}, and N_{IQbits} denote the number of supported layers in access link, the number of tones per orthogonal frequency-division multiplexing (OFDM) symbol in FH link, and the combined bit-width used for representing each I/Q sample in FH link, respectively. τ_{sym} represents the symbol duration of each OFDM symbol. CP_{oh} denotes the cyclic prefix (CP) overhead and FH_{oh} the FH overhead.

Several key factors contribute to the FH rate requirement, including the number of layers, the number of tones, and the combined bit-width of I/Q samples. Notably, compression algorithms such as block floating point compression and modulation compression introduced in [8] can help reduce the required FH data rate, as reflected in Table 1. For instance, different values of $N_{IQbits} = (32, 18, 6)$ are used for the uncompressed case, block floating point compression case, and modulation compression case, respectively. Assuming a 2.5 GHz bandwidth allocated for WFH, a total spectrum efficiency of 18 bps/Hz is required for the compressed case, while 31.2 bps/Hz is necessary for the uncompressed case. For clarity and reference, the major variables used in subsequent sections are listed in Table 2.

TABLE 1. Fronthaul requirements and link budget for the deployment scenario considered in Fig. **1**.

Access (Uu) links			Fronthaul (FH) links		Derived FH data rate requirements for Uu links operating at FR1 or FR2 respectively	
Band	Parameter	Value	Parameter	Parameter	FH I/Q compression	Required FH data rate (DL/UL)
FR1	Total bandwidth (BW)	400 MHz	Carrier frequency	80 GHz	Uncompressed SO 7-2x	FR1(Uu), FH DU/UL: 52 Gbps
	Number of layers	4	Fronthaul coverage	10 to 500 m		
	Occupied BW	0.95	Path loss (LOS)	91 to 132 dB		FR2(Uu), FH DU/UL: 78 Gbps
	Max modulation	256 QAM	Carrier BW	2.5 GHz		
	Fronthaul overhead	15%	Number of layers (two polarization)	8	Block floating point based compression [8], SO 7-2x	FR1(Uu), FH DU/UL: 30 Gbps
FR2	Total bandwidth (BW)	1200 MHz	Max modulation	256 QAM		
	Number of layers	2	Number of multiplexed RUs per DU	2 to 4		FR2(Uu), FH DU/UL: 45 Gbps
	Occupied BW	0.95	Number of WFH panels	8		
	Max modulation	64 QAM	Number of elements per antenna panel	128 (16 by 8)	Modulation compression [8], downlink only, SO 7-2x	FR1(Uu), FH DL: 10 Gbps
	Fronthaul overhead	15%	Effective isotropic radiated power (EIRP) per antenna panel	~55 dBm		FR2(Uu), FH DL: 15 Gbps

III. OPTIMIZING LOS-MIMO FOR ROBUST WIRELESS FRONTHAULING

In lower frequency ranges (e.g., sub-6 GHz), traditional MIMO techniques like massive MIMO rely on exploiting rich scatterings in the non-line-of-sight (NLOS) propagation environment to achieve spatial multiplexing gain [11]. However, in these frequency bands, the large bandwidth required to meet high fronthaul data rates (as indicated in Table 1) is not readily available. Furthermore, employing a very large number of antennas would result in impractically large array sizes at lower frequency ranges.

On the other hand, in mmWave and higher frequency bands, LOS-MIMO techniques leverage the curvature of the wavefront, observable within the receiver or transmitter aperture, to create spatial degrees of freedom [12]. By optimizing the antenna configuration (e.g., aperture size and separation) and using beamforming (both analog and digital), LOS-MIMO with phased arrays achieves high rank and high-capacity communication [13], facilitated by the availability of a large bandwidth. As a result, LOS-MIMO at mmWave bands benefits not only from a higher signal-to-noise ratio (SNR) compared to NLOS propagation but also gains from high-rank spatial multiplexing, leading to improved system performance.

Instead of adopting the massive MIMO approach in mmWave bands, we choose to limit the number of radio chains (antenna panels) to a relatively small number. Each antenna panel consists of a large number of antenna elements (e.g., 128), enabling us to implement hybrid analog-digital beamforming [14] and achieve higher effective isotropic radiated power (EIRP) per antenna panel. The approach of utilizing a smaller number of antenna panels with a larger number of antenna elements per panel strikes a balance between cost-effectiveness and performance, allowing us to optimize the system's performance for WFH while minimizing manufacturing and deployment costs.

In this section, we will begin by presenting theoretical insights into LOS-MIMO, specifically focusing on the achievable DoF in LOS-MIMO. This analysis will provide a fundamental understanding of the relationship between spatial multiplexing gain (which results from DoF) and various factors such as aperture size, operation distance, and array mis-alignment. Subsequently, we will introduce a tailored design for WFH that involves optimizing the required number of antennas, aperture size, and antenna separation to achieve the desired degree of freedom. The primary objective of this design is to strike a well-balanced combination of robust performance, sufficient spectrum efficiency, and cost-effectiveness for WFH applications.

A. LOS-MIMO: THEORETICAL BACKGROUND

LOS-MIMO is based on exciting an electromagnetic wave in a transmitter (Tx) aperture and capturing the field in a receiver (Rx) aperture. Common shapes for these apertures include linear, rectangular (planar), and circular apertures. However, this paper will focus specifically on linear apertures. We start with the most general case where the Tx aperture is excited by a space continuous waveform and at the Rx-aperture a space continuous waveform is picked up and processed. Later we come to the more practical case where discrete antenna elements are placed in the Tx and Rx aperture and signals are fed into or picked from those antenna elements. This represents space discrete processing, and its effects are studied below. The antenna elements can also be generalized to be antenna panels allowing for hybrid beamforming. The discretization of the apertures can occur in either a uniform or non-uniform fashion, and the paper will provide examples of both cases. In the literature,

TABLE 2. List of key variables and descriptions.

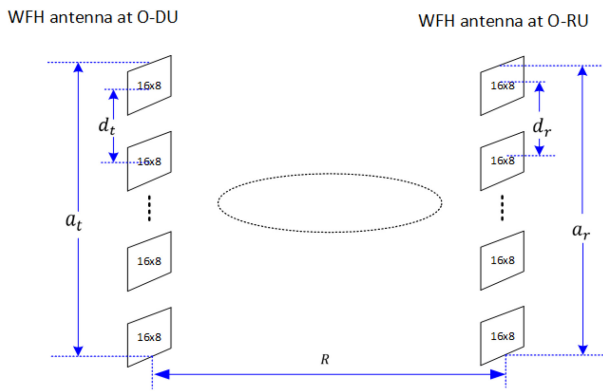| Variable	Description	Variable	Description
λ	wavelength	k	angular wave number ($k = \frac{2\pi}{\lambda}$)
d_t	Tx antenna spacing	d_r	Rx antenna spacing
a_t	Tx antenna aperture size	a_r	Rx antenna aperture size
$\underline{e}_t$	unit vector of Tx aperture direction	$\underline{e}_r$	unit vector of Rx aperture direction
$\underline{e}_R$	unit vector parallel to the line connecting Tx and Rx center points	$\underline{P}_R$	projection operator onto the plane orthogonal to $\underline{e}_R$
a_t^{eff}	effective Tx antenna aperture size	a_r^{eff}	effective Rx antenna aperture size
$d\,(x_r, x_t)$	distance between point x_r and x_t	$E\,(x_r)$	electric field at point x_r
R	Tx and Rx distance	N_{DoF}	the number of degrees of freedom
N	the number of antennas/panels	L	a threshold of degrees of freedom
N_t	the number of Tx antennas/panels	N_r	the number of Rx antennas/panels
μ	the misalignment factor	F_c	carrier frequency
R_{min}	Tx-Rx minimum distance	R_{max}	Tx-Rx maximum distance
N_{tap}	the number of channel taps	K	FFT size for frequency domain channel
ϵ^2	power percentage of LOS path	N_{elem}	total number of antenna elements
N_c	the number of samples for encoder output	K_c	the number of samples for encoder input

FIGURE 2. Multi-panel uniform linear array (ULA) for WFH.

FIGURE 3. Linear Tx and Rx apertures in arbitrary orientation with continuous excitation and reception.

the associated architectures are referred to as uniform linear arrays (ULA) (see Fig. 2) or non-uniform arrays (NULA).

The performance of LOS-MIMO depends on the DoF (channel rank) of the mapping between the excitation in the Tx aperture and the resulting electric field (E-field) in the Rx aperture. In the following the DoF for continuous linear apertures are derived, the effects of spatial sampling of those apertures by antenna elements/panels are analyzed and then different designs for the fronthaul use case are proposed and discussed. The objective is to maintain a given minimum rank with the smallest number of antenna panels. The first part follows the derivation in [15] but is more tailored to highlighting the effects of misalignment of the linear arrays.

Fig. 3 shows linear Tx and Rx apertures with the respective sizes a_t and a_r, separated by the distance R. Let $\underline{e}_R$ denote the unit vector parallel to the line connecting the center points of the apertures. The unit vectors $\underline{e}_t$ and $\underline{e}_r$ denote the directions of the aperture axes, while x_t and x_r are the spatial coordinates associated to the apertures. In this analysis, we do not assume $\underline{e}_t$ and $\underline{e}_r$ to be exactly parallel to each other, nor do they need to be orthogonal to $\underline{e}_R$. Furthermore, $\underline{e}_t$, $\underline{e}_r$, and $\underline{e}_R$ do not necessarily lie in
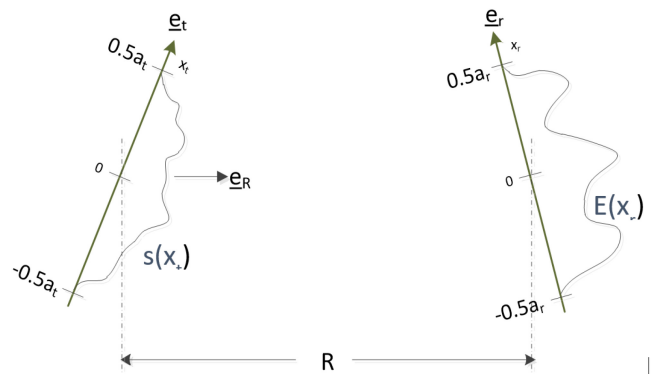
the same plane. With this general approach, we can access the influence of any misalignment of the apertures. Let $s(x_t)$ be the excitation or transmit signal of the Tx aperture, and $E(x_r)$ be the electric field in the Rx aperture. We assume $s(x_t)$ is proportional to an electric current density along the Tx aperture, such that we have

$$E(x_r) = \int_{-a_t/2}^{a_t/2} \frac{e^{-jkd(x_r, x_t)}}{d(x_r, x_t)} \cdot s(x_t) dx_t, \qquad (2)$$

where $d(x_r, x_t)$ is the distance between the points indicated by x_r and x_t of the Tx and Rx aperture, and $k = \frac{2\pi}{\lambda}$ with λ being the wavelength. Equation (2) has the same structure as the Fresnel diffraction integral [16] and therefore its further evaluation involves two approximations. For the denominator $d(x_r, x_t) \approx R$ is used and for the numerator $d(x_r, x_t)$ is approximated by its Taylor expansion truncated after the quadratic term

$$d(x_r, x_t) \approx R + \underline{e}_R^T (\underline{e}_r x_r - \underline{e}_t x_t) + \frac{\underline{e}_r^T \underline{P}_R \underline{e}_r}{2R} x_r^2$$
$$+ \frac{\underline{e}_t^T \underline{P}_R \underline{e}_t}{2R} x_t^2 - \frac{\underline{e}_r^T \underline{P}_R \underline{e}_t}{R} x_r x_t, \qquad (3)$$

where $\underline{P}_R = \underline{1} - \underline{e}_R\underline{e}_R^T$ is the projection operator onto the plane orthogonal to $\underline{e}_R$. Note that underlined letters are used to represent vectors. It turns out that for DoF analysis only the last term is relevant. To highlight that effect, we define

$$\theta_t(x_t) := -jkR + jk\underline{e}_R^T\underline{e}_t x_t - jk\frac{\underline{e}_t^T\underline{P}_R\underline{e}_t}{2R}x_t^2, \tag{4}$$

$$\theta_r(x_r) := jk\underline{e}_R^T\underline{e}_r x_r + jk\frac{\underline{e}_r^T\underline{P}_R\underline{e}_r}{2R}x_r^2, \tag{5}$$

and obtain

$$E(x_r) \cdot Re^{j\theta_r(x_r)} = \int_{-a_t/2}^{a_t/2} e^{j\theta_t(x_t)} s(x_t)e^{jk\frac{\underline{e}_r^T\underline{P}_R\underline{e}_t}{R}x_r x_t}dx_t. \tag{6}$$

The phase rotations $e^{j\theta_t(x_t)}$ and $e^{j\theta_r(x_r)}$ represent unitary transformations and therefore have no influence on the singular values of the mapping between s and E. The factor R scales down all singular values by R, and has no influence on the singular value spread and the number of DoF. With $\widetilde{E}(x_r) \triangleq E(x_r) \cdot Re^{j\theta_r(x_r)}$ and $\widetilde{s}(x_t) \triangleq e^{j\theta_t(x_t)} \cdot s(x_t)$ we simply obtain

$$\widetilde{E}(x_r) = \int_{-a_t/2}^{a_t/2} \widetilde{s}(x_t) \cdot e^{jk\frac{\underline{e}_r^T\underline{P}_R\underline{e}_t}{R}x_r x_t}dx_t, \tag{7}$$

which means that the spatial Rx signal is the Fourier Transform of the spatial transmit signal $\widetilde{s}(x_t)$, if we define $\widetilde{s}(x_t)$ to be zero outside of the Tx aperture. If $\widetilde{s}$ were a function in time, the Tx aperture would act as a time limitation of $\widetilde{s}$, while $\widetilde{E}(x_r)$ were its Fourier Transform at the frequency

$$f = \frac{|\underline{e}_r^T\underline{P}_R\underline{e}_t|}{\lambda R}x_r. \tag{8}$$

Since the size of the Rx aperture is limited to a_r, the receiver has only access to the contents of the band $\left(\frac{|\underline{e}_r^T\underline{P}_R\underline{e}_t|}{\lambda R}\right) \cdot [-\frac{a_r}{2}\frac{a_r}{2}]$, that is, the LOS-MIMO system contains the mathematical equivalent of a time and band limitation. Therefore, results from traditional communication systems limited in time and frequency can be readily applied to our LOS-MIMO system. The singular values and associated eigenfunctions of such a traditional system have been thoroughly investigated by [17], [18]. Their famous work has shown that most of the singular values are either close to 0 or 1, while the few remaining singular values are between 0 and 1. The number of singular values that are close to 1 can be approximated by the time bandwidth product. The accuracy of this approximation increases with the value of the time bandwidth product and a more precise characterization is given in [15]. For the LOS-MIMO case for linear apertures we have a "time limitation" of a_t and a frequency limitation of $\frac{|\underline{e}_r^T\underline{P}_R\underline{e}_t| \cdot a_r}{\lambda R}$. The time bandwidth product and the number of DoF comes to

$$N_{DoF} = \left|\underline{e}_r^T\underline{P}_R\underline{e}_t\right|\frac{a_r a_t}{\lambda R}. \tag{9}$$

As the distance R increases, a larger aperture product $a_r a_t$ is required to maintain a given number of DoF N_{DoF} or rank. Therefore, from a design perspective, the aperture size is determined by the largest distance one needs to support. To reduce the required size, operating at a lower wavelength λ (higher carrier frequency) can be considered. Concerning aperture alignment, the term $|\underline{e}_r^T\underline{P}_R\underline{e}_t|$ reaches its highest value of 1 if and only if both aperture axes are parallel and orthogonal to $\underline{e}_R$. In the deployment of LOS-MIMO for fronthaul, achieving perfect alignment of the apertures may not always be feasible, especially when one aperture at the DU needs to communicate with several apertures located at different RUs mounted at various heights. Additionally, environmental factors such as wind can cause apertures to deviate from perfect alignment. However, the term $|\underline{e}_r^T\underline{P}_R\underline{e}_t|$ indicates that small deviations from perfect alignment only cause a mild degradation of N_{DoF}. Also, from (7) one can see that a misaligned system has the same input/output behavior as an aligned system operating at a slightly larger distance of $\frac{R}{|\underline{e}_r^T\underline{P}_R\underline{e}_t|}$. Hence, robustness against misalignment is achieved by robustness against changes in distances R.

1) EFFECTS OF SPACE-DISCRETIZATION

We start looking at uniformly sampling the Tx aperture. Any excitation $\widetilde{s}(x_t)$ based on eigenfunctions of the dominant singular values of the mapping of eq. (2) will be such that the associated $\widetilde{E}(x_r)$ is concentrated to the Rx aperture. If we replace the space continuous excitation $\widetilde{s}_c(x_t)$ by the space discrete excitation $\widetilde{s}_d(x_t) = d_t \sum_n \widetilde{s}_c(nd_t) \cdot \delta(x_t - nd_t)$ with d_t denoting the spacing of antennas in the Tx aperture (see Fig. 2), we obtain for its Fourier Transform (using the Poisson sum formula)

$$\widetilde{S}_d(f) = \mathcal{F}\left\{\widetilde{S}_d(x_t)\right\} = \sum_m \widetilde{S}_c\left(f - \frac{m}{d_t}\right), \tag{10}$$

where $\widetilde{S}_c(f)$ is the Fourier Transform of $\widetilde{s}_c(x_t)$. With $\widetilde{E}_c(x_r)$ and $\widetilde{E}_d(x_r)$ being the electric field associated to $\widetilde{s}_c(x_t)$ and $\widetilde{s}_d(x_t)$ we finally obtain

$$\begin{aligned}\widetilde{E}_d(x_r) &= \widetilde{S}_d\left(\frac{|\underline{e}_r^T\underline{P}_R\underline{e}_t|}{\lambda R}x_r\right) \\ &= \sum_m \widetilde{S}_c\left(\frac{|\underline{e}_r^T\underline{P}_R\underline{e}_t|}{\lambda R}x_r - \frac{m}{d_t}\right) \\ &= \sum_m \widetilde{E}_c\left(x_r - m\frac{\lambda R}{d_t|\underline{e}_r^T\underline{P}_R\underline{e}_t|}\right). \end{aligned} \tag{11}$$

We experience a repetition of the original waveform (spatial aliasing) at multiples of $\frac{\lambda R}{d_t|\underline{e}_r^T\underline{P}_R\underline{e}_t|}$. This spatial aliasing can also be viewed as the result of grating lobes. Such lobes are known to come from arrays which have an antenna spacing larger than $\frac{\lambda}{2}$. The E-field $\widetilde{E}_d(x_r)$ to equal the desired field $\widetilde{E}_c(x_r)$ within the Rx-aperture, the terms for $m \neq 0$ must vanish for $|x_r| \leq \frac{a_r}{2}$. Therefore, the spatial shift of the aliasing products must exceed the aperture size a_r

$$a_r \leq \frac{\lambda R}{d_t|\underline{e}_r^T\underline{P}_R\underline{e}_t|} \Leftrightarrow d_t \leq \frac{\lambda R}{a_r|\underline{e}_r^T\underline{P}_R\underline{e}_t|}, \tag{12}$$

which is the Nyquist criterion for spatial aliasing. It is important to know what happens when it is violated. Then the period length of $\tilde{E}_d(x_r)$ is less than the aperture size a_r and in the absence of thermal noise the receiver can obtain all available information from evaluating the E-field in an interval of length

$$a_r^{eff} := \frac{\lambda R}{d_t \left| \underline{e}_r^T \underline{P}_R \underline{e}_t \right|}, \qquad (13)$$

which can be viewed as the effective (reduced) Rx aperture. Hence the N_{DoF} equals the N_{DoF} of a system that operates with the aperture sizes a_t and a_r^{eff}. We can generalize (9) to include the influence of Tx array sampling

$$N_{DoF} = \left| \underline{e}_r^T \underline{P}_R \underline{e}_t \right| \frac{\min\left(a_r^{eff}, a_r\right) \cdot a_t}{\lambda R}$$
$$= \min\left(\left| \underline{e}_r^T \underline{P}_R \underline{e}_t \right| \frac{a_r a_t}{\lambda R}, N_t \right), \qquad (14)$$

where $N_t = \frac{a_t}{d}$. N_t can be interpreted as the number of Tx antenna elements or panels. In the presence of thermal noise, the receiver will also use the waveform received outside of the effective receiver aperture a_r^{eff} for maximum ratio combing (MRC) leading to enhanced SNRs. However, N_{DoF} or the rank will remain the same as in (14) while the absolute values of all singular values will increase.

For space discrete processing at the receive aperture one can derive the Nyquist criterion along the same lines and obtain

$$d_r \leq \frac{\lambda R}{a_t \left| \underline{e}_r^T \underline{P}_R \underline{e}_t \right|}, \qquad (15)$$

where d_r is the antenna spacing within the Rx aperture. If the criterion is violated the achievable number of degrees of freedom is that of a system with a reduced Tx aperture size

$$a_t^{eff} := \frac{\lambda R}{d_r \left| \underline{e}_r^T \underline{P}_R \underline{e}_t \right|}. \qquad (16)$$

Activation of the Tx aperture outside of an interval of length a_t^{eff} will increase the size of the dominant singular values but their number remains the same. The formula for N_{DoF} that includes Rx aperture sampling becomes

$$N_{DoF} = \left| \underline{e}_r^T \underline{P}_R \underline{e}_t \right| \frac{\min(a_{teff}, a_t) \cdot a_r}{\lambda R}$$
$$= \min\left(\left| \underline{e}_r^T \underline{P}_R \underline{e}_t \right| \frac{a_r a_t}{\lambda R}, N_r \right), \qquad (17)$$

where $N_r := \frac{a_r}{d_r}$ can be interpreted as the number of Rx antenna elements or panels. If both, Tx and Rx sampling occur, one expects that N_{DoF} is determined by the superposition of the effects of (15) and (17) which would lead to

$$N_{DoF} = \left| \underline{e}_r^T \underline{P}_R \underline{e}_t \right| \frac{\min\left(a_t^{eff}, a_t\right) \cdot \min\left(a_r^{eff}, a_r\right)}{\lambda R}$$
$$= \min\left(\left| \underline{e}_r^T \underline{P}_R \underline{e}_t \right| \frac{a_r a_t}{\lambda R}, N_t, N_r, \frac{\lambda R}{\left| \underline{e}_r^T \underline{P}_R \underline{e}_t \right| d_t d_r} \right). \quad (18)$$

However, there is one peculiarity to consider. With Tx discretization, two points in the Rx aperture that are $\frac{\lambda R}{d_t \left| \underline{e}_r^T \underline{P}_R \underline{e}_t \right|}$ apart from each other have the same E-field $\tilde{E}_d(x_r)$. Hence, for a thought experiment, an antenna at x_r and can be shifted to $x_r + v \frac{\lambda R}{d_t \left| \underline{e}_r^T \underline{P}_R \underline{e}_t \right|}$ without affecting N_{DoF}, whereby v is an integer. Hence, without penalty, one can shift all receive antennas from locations $x_r(n)$ to new locations $\tilde{x}_r(n)$ where all $\tilde{x}_r(n)$ are inside of an interval I_r of length $a_r^{eff} := \frac{\lambda R}{d_t \left| \underline{e}_r^T \underline{P}_R \underline{e}_t \right|}$. Formally, with $I_r := [x_0 \quad x_0 + a_r^{eff})$ we have $\tilde{x}_r(n) = (x_r(n) - x_0) \mod a_r^{eff} + x_0$, where x_0 is an arbitrary offset. The antenna spacing associated with the new locations $\tilde{x}_r(n)$ could be smaller than d_r since now all antennas are crowded into I_r. The benefit of that is a larger a_{teff} (see eq. (16)). To illustrate the point, consider that R is such that $a_r^{eff} = (m + \frac{1}{2}) \cdot d_r$, where m is some integer. Then for $x_r(n) \in [x_0 + a_r^{eff} \quad x_0 + 2a_r^{eff})$ we have $\tilde{x}_r(n) = x_r(n) - a_r^{eff} = x_r(n) - (m + \frac{1}{2})d_r$ and $\tilde{x}_r(n)$ is not on the original sampling grid (occupied by $x_r(n)$) but half way between two original sampling points. All $x_r(n) \in [x_0 + 2a_r^{eff} \quad x_0 + 3a_r^{eff})$ end up at $\tilde{x}_r(n) = x_r(n) - 2a_r^{eff} = x_r(n) - (2m+1)d_r$ and lie on the original sampling grid. Continuing this line of thinking one arrives at the conclusion that the spacing associated to $\tilde{x}_r(n)$ is $d_r/2$. This assumes that there enough antennas at $x_r(n)$ outside of I_r such that within I_r all points of a grid with spacing $d_r/2$ are occupied by a $\tilde{x}_r(n)$. This situation occurs at distances $R_{m+\frac{1}{2}} := (m + \frac{1}{2}) \cdot \frac{d_r d_t \left| \underline{e}_r^T \underline{P}_R \underline{e}_t \right|}{\lambda}$. Likewise at distances

$$R = R_{m+\frac{p}{q}} := \left(m + \frac{p}{q} \right) \cdot \frac{d_r d_t \left| \underline{n}_r^T \underline{P}_R \underline{e}_t \right|}{\lambda}, \qquad (19)$$

the effective spacing d_{reff} associated to $\tilde{x}_r(n)$ is

$$d_{reff} = \begin{cases} \frac{d_r}{q}, & \text{if } p \text{ and } q \text{ are coprime and } p \neq 0, \\ d_r, & \text{if } p = 0, \end{cases} \qquad (20)$$

and therefore

$$N_{DoF}\left(R_{m+\frac{p}{q}}\right) = \begin{cases} qm + p, & \text{if } p \text{ and } q \text{ are coprime, } p \neq 0, \\ m, & \text{if } p = 0. \end{cases} \qquad (21)$$

The distances R_m and $R_{m+\frac{1}{2}}$ or $R_{m+\frac{p}{q}}$ are typically close together and N_{DoF} may jump by a factor of 2 or even q for small changes of R. Recall that this situation only happens for $a_r^{eff} < a_r$ and $a_t^{eff} = \frac{\lambda R}{d_r \left| \underline{e}_r^T \underline{P}_R \underline{e}_t \right|} < a_t$. Typically, this situation may be observed for small distances R. Then (19) needs to be revised to

$$N_{DoF} = \min\left(\left| \underline{e}_r^T \underline{P}_R \underline{e}_t \right| \frac{a_r a_t}{\lambda R}, N_t, N_r, \frac{\lambda R}{\left| \underline{e}_r^T \underline{P}_R \underline{e}_t \right| d_t d_{reff}} \right). \quad (22)$$

However, one approach of making the fronthaul link performance robust relative to changes in R consists of not taking advantage of the "windfall" gains of the factor q for certain distances and instead make sure that the N_{DoF} from (19) is larger than a desired threshold. In the following we will refer to it as $N_{DoF,LB}$:

$$N_{DoF,LB} = \min\left(\left| \underline{e}_r^T \underline{P}_R \underline{e}_t \right| \frac{a_r a_t}{\lambda R}, N_t, N_r, \frac{\lambda R}{\left| \underline{e}_r^T \underline{P}_R \underline{e}_t \right| d_t d_r} \right). \quad (23)$$

TABLE 3. Designs of ULA and NULA.

Case	Description	Number N of antennas (radio chains)	Aperture size
1	Avoid Tx and Rx aperture reduction for all R	$L \cdot \frac{R_{\max}}{R_{\min}}$	$\sqrt{\frac{\lambda L R_{\max}}{\mu}}$
2	Allow aperture reduction for Tx and Rx but maintain $N_{DoF,LB} \geq L$	$L \cdot \sqrt{\frac{R_{\max}}{R_{\min}}}$	
3	Value for N enforced. Small N may cause $N_{DoF,LB} < L$ for small R.	N	
4	Quadratic NULA - improve case 3 by modest deviation from uniform spacing	N	

From there we can derive

$$d_t d_r \leq \frac{\lambda R}{N_{DoF,LB} |\underline{e}_r^T \underline{P}_R \underline{e}_t|}. \tag{24}$$

This expression is similar but not equal to one found in [12]. The discrepancy is due to a difference in objectives. In [12] orthogonality of the rows or columns of the channel matrix is aimed for while here the goal is to capture the relationship between antenna spacing and $N_{DoF,LB}$.

2) TAILORED DESIGNS FOR FRONTHAUL

In practical fronthaul deployment, it is expected that the same ULA/NULA design is used for all links of the coverage area of an operator. For sake of a realistic example, we assume that links must bridge different distances R between $R_{\min} = 10$ m and $R_{\max} = 500$ m. Our goal is to maintain the number of DoF N_{DoF} above a threshold L for all R, where L falls within the range of 1.5 to 3. We use a fractional L to take into account that in a band and time-limited system, the achievable rank is slightly larger than the time-bandwidth product, as previously shown in [15] and [18].

To evaluate the designs, we focus on two main factors: (1) the number N of antennas/panels, which directly corresponds to the number of radio-chains and is a significant cost driver, and (2) the aperture size, which affects manufacturing and deployment costs. For simplicity, we assume that Tx and Rx employ the same array. To streamline the discussion, we introduce the misalignment factor $\mu := |\underline{e}_r^T \underline{P}_R \underline{e}_t|$. In the following, four design cases will be discussed, with the last two cases being relevant for fronthaul links. The results are summarized in Table 3.

In the **first approach**, we want to avoid aperture reductions for all distances R. For the aperture size $a_t = a_r = a$, we need $\frac{\mu a^2}{\lambda R} \geq L$ for all R. The smallest aperture size to satisfy this requirement is given by

$$a = \sqrt{\frac{\lambda L R_{\max}}{\mu}}. \tag{25}$$

To ensure that both Tx and Rx Nyquist criteria are met, we set the antenna spacing as $d_t = d_r = d$, ensuring that $d \leq \frac{\lambda R}{a\mu}$ for all R. The most stringent requirement occurs at $R = R_{\min}$, yielding

$$d = \frac{\lambda R_{\min}}{a\mu}. \tag{26}$$

The number N of antennas can be calculated as

$$N = \frac{a}{d} = \frac{\mu a^2}{\lambda R_{\min}} = L \cdot \frac{R_{\max}}{R_{\min}}. \tag{27}$$

With the assumptions above, we find that N ranges from 75 to 150 antennas, which is quite high. For the calculation of N_{DoF}, we use the fact that the aperture is not reduced and obtain

$$N_{DoF,LB}(R) = N_{DoF}(R) = \frac{\mu a^2}{\lambda R} = L \cdot \frac{R_{\max}}{R}. \tag{28}$$

At $R = R_{\min}$, we get $N_{DoF} = L \cdot \frac{R_{\max}}{R_{\min}}$, which is 75 to 150, much more than is needed, especially considering that at these small distances, the pathloss is much smaller than at the largest distance.

One possible reason for the high number of antennas is the dependence of spacing d on the Nyquist criterion for the minimum distance $R = R_{\min}$. In [19], an alternative approach is suggested, involving making a monotonically increasing function of R. This design allows for larger spacing d and a smaller number of antennas N. However, during deployment, each array would have to be tilted away from the upright orientation, depending on the link distance. This may pose challenges due to space limitations and could increase deployment costs. Additionally, it complicates scenarios where a single array at a DU needs to maintain links with several other arrays at RUs.

In the **second approach**, we reduce N by allowing a reduction of aperture sizes by aliasing. Thereby we keep $N_{DoF,LB}(R)$ above L. The aperture size a is given by (20). The reduced aperture size at distance R is

$$a_{red} = \min\left(\frac{\lambda R}{\mu d}, \sqrt{\frac{\lambda L R_{\max}}{\mu}}\right), \tag{29}$$

leading to an $N_{DoF,LB}$ of

$$N_{DoF,LB}(R) = \frac{\mu a_{red}^2}{\lambda R} = \min\left(\frac{\lambda R}{\mu d^2}, L \frac{R_{\max}}{R}\right). \tag{30}$$

The condition $N_{DoF,LB}(R) \geq L$ leads to $d = \sqrt{\lambda R_{\min}/\mu L}$ requiring

$$N = L \cdot \sqrt{\frac{R_{\max}}{R_{\min}}} \tag{31}$$

antennas, which comes to $11 \ldots 22$. This is an important improvement relative to the first case but still a little high. With this choice of d, we get

$$N_{DoF,LB}(R) = \min\left(L\frac{R}{R_{\min}}, L\frac{R_{\max}}{R}\right), \qquad (32)$$

that is, for $R \le \sqrt{R_{\min} \cdot R_{\max}}$ the lower bound of the number of degrees of freedom grows linearly with R and for the rest $N_{DoF}(R)$ falls with $\frac{1}{R}$. The maximum of $N_{DoF}(R)$ equals N.

In the **third case**, we just choose N. For $N_{DoF,LB}(R)$ we obtain

$$N_{DoF,LB}(R) = \min\left(R\frac{N^2}{L \cdot R_{\max}}, L\frac{R_{\max}}{R}\right), \qquad (33)$$

whereby $L = \frac{\mu a^2}{\lambda R_{\max}}$. Like in case 2, $N_{DoF,LB}$ grows linearly for $R \le R_{\max} \cdot \frac{L}{N}$ and afterwards it falls off with $\frac{1}{R}$. Its maximum is again equal to N. $N_{DOF,LB}$ may drop to small values below 1 for $R = R_{\min}$. However, since the pathloss is smaller for small distances R, a satisfactory performance can still be achieved (see figures 4(a) and 4(b)).

In the **fourth case**, we improve upon case 3. Fig. 4(a) shows the performance of a ULA designed by the method of case 3 with $N = 8$ antennas. For small distances, $N_{DoF,LB}$ can become quite small, as seen in Fig. 5(a). However, the associated "poor" performance is only experienced at a few discrete distances $R_{m+\frac{p}{q}}$. Here we want to address this issue and improve the performance. The root cause for the poor performance has been outlined in Section III-A1 (19)-(21). At those specific distances R, spatial aliasing causes a spatially periodic signal at the Rx aperture. If two Rx-antennas are separated by the period length or a multiple thereof, they will deliver the same signal (neglecting thermal noise). As a result, the N_{DoF} value shrinks. The situation is most dramatic if the period length equals the Rx antenna spacing. Then all Rx antennas will deliver the same signal and $N_{DoF} = 1$. In Fig. 5(a) the leftmost marked red dot shows the performance for that situation. If the aliasing period equals two antenna spacings, we are left with only two antennas delivering independent signals and hence $N_{DoF} = 2$. The second red dot in Fig. 5(a) corresponds to that case.

Indeed, to avoid the problems caused by spatial aliasing, we can design the Rx antennas to not be exactly uniformly spaced. For this approach, we assume the Tx array to remain uniformly spaced. Then, if the spatial period length of the Rx-signal equals the spacing of two Rx-antennas it does not simultaneously equal the spacing of another antenna pair and a dramatic dip of N_{DoF} is avoided. Here we simply assume an antenna spacing that grows linearly across the array:

$$x_r(n+1) - x_r(n) = \left(1 - \gamma + \gamma \cdot \frac{n}{\frac{N}{2} - 1}\right) \cdot \frac{a_r}{N},$$
$$n = 0 \ldots N - 2, \qquad (34)$$

where $x_r(n)$ is the location of the Rx antenna n. From simulations one can find that a good choice for γ is between 0.2
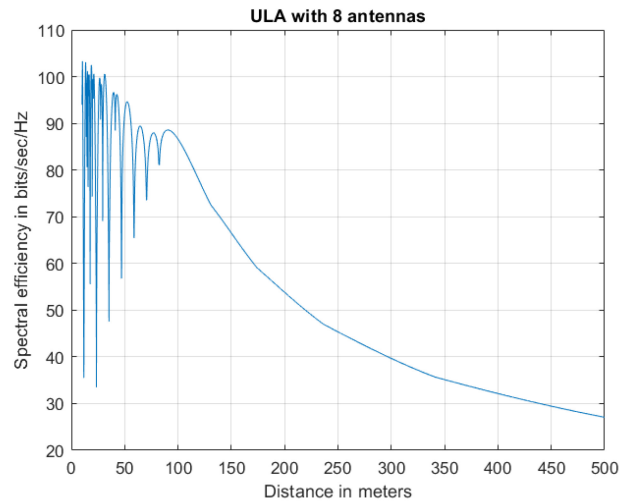
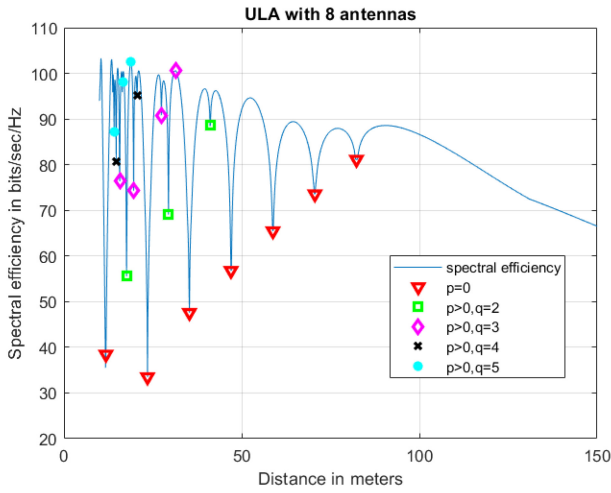(a) Spectrum efficiency vs distance
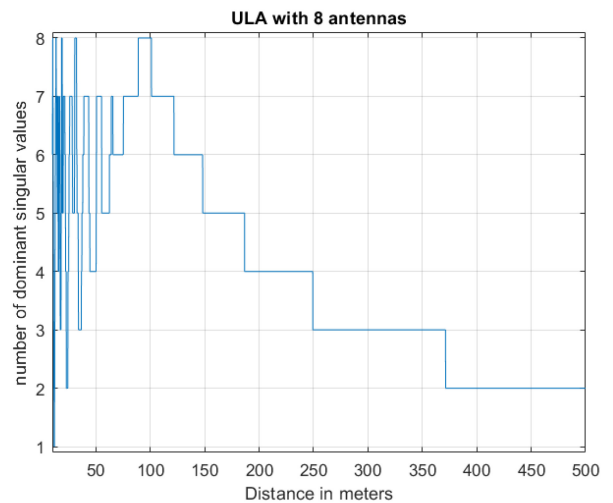
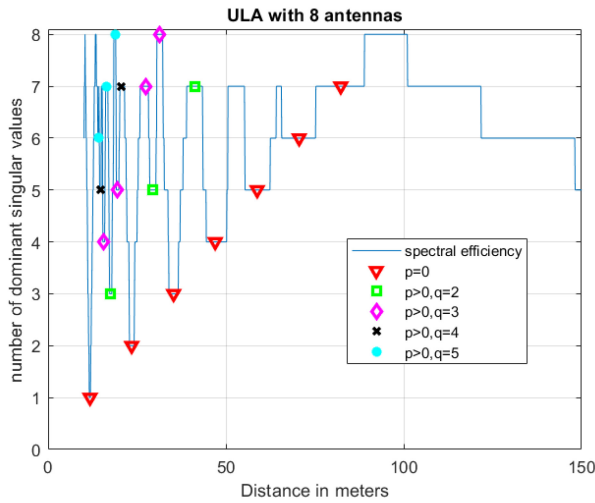

(b) Number of dominant singular values vs distance

FIGURE 4. Performance of ULAs at Tx and Rx with 8 antennas.

and 0.4. The Rx antenna locations $x_r(n)$ depend quadratically on n. Hence, we refer to this as quadratic spacing and label the array as quadratic spaced linear array (QLA). Simulations confirm that the performance dips indeed vanish for the QLA (see Fig. 6(a)). With the Tx aperture still linearly spaced, the deployment would require two array types, a ULA and QLA. When converting the Tx array to a QLA the spatial signal in the Rx array will no longer be periodic and it is not straightforward to know how aliasing expresses itself. Nevertheless, simulations show that the performance improves when QLAs are also used for Tx (see Fig. 6(a)). The details for this behavior are subject to further research.

The idea to use a NULA to enable satisfactory performance of LOS-MIMO over a plurality of distances R was pioneered in [18], where a full search over all possible antenna locations has yielded a design where the minimum spectral efficiency over all R has been maximized. The
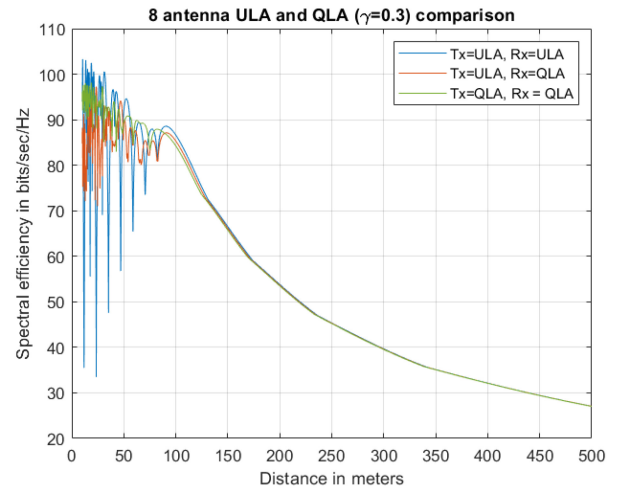
(a) Spectrum efficiency vs distance

(a) Spectrum efficiency for 8-antenna ULA and QLA

(b) Number of dominant singular values vs distance

(b) Spectrum efficiency for QLA with different N

FIGURE 5. Illustration of distances R_{m+p} and associated performance dips for ULA designed by case 3.
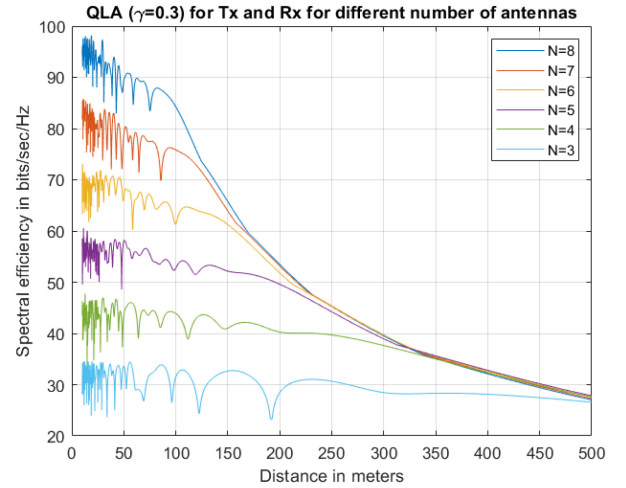
FIGURE 6. Comparison between ULA and QLA.

approach here does not require a full search. It provides some insight into the reasons why non-uniform spacing provides benefits and the derived method can be easily used when a larger number of antennas is involved.

3) SIMULATION RESULTS FOR LOS-MIMO

We now show some simulations using the FH parameters described in Table 1 and 4. Those parameters are based on design case 3. We strive for $L = 1.5$, which at an assumed carrier frequency of 80 Ghz and an R_{max} of 500 m leads to an aperture size of $a = 1.68$ m. We choose the number N of antennas such that a satisfactory spectral efficiency is obtained for small distances, which per simulations leads to $N = 8$ resulting in an antenna spacing of $d = \frac{a}{N} = 0.21$ m. We assume that the Tx array maintains the same EIRP for all distances R and that the power of self-noise is -30 dBc (see details in Section III-B).

Fig. 4(a) shows the spectral efficiency of the same 8-panel ULA array as a function of the distance between Tx and Rx array. For distances R above $R_{max} \cdot \frac{L}{N} = 93.75$ m, there is no spatial aliasing within the apertures and hence the discretization of the apertures does not limit the performance. Fig. 4(b) shows the number of dominant singular values as a measure for N_{DoF}. Here, a singular value is considered dominant if it exceeds one half of the largest singular value. For distances above 93.75 m, one can see the $\frac{1}{R}$ decay of N_{DoF}. For distances below 93.75 m aliasing reduces the Tx and Rx apertures. One can identify the linear increase of the $N_{DoF,LB}(R)$ curve (see red triangles in Fig. 5(b)) which is the lower envelope of the $N_{DoF}(R)$ curve.

To investigate the performance dips for lower distances, Fig. 5 contains a zoomed in version of Fig. 4. As one can see, all performance dips can be explained by the phenomena discussed around (19). The most severe performance dips (marked by the red triangles) occur when the period length
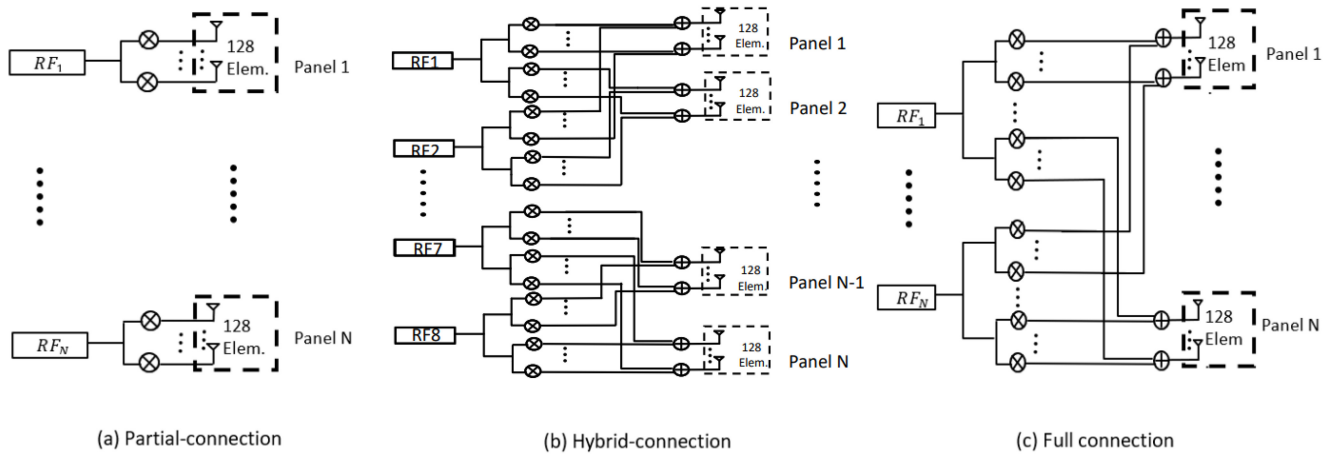
FIGURE 7. Array architecture: partial-, hybrid-, and full-connection.

of Rx signals equals m times the antenna spacing, where $m = 1..N − 1$. Fig. 5(b) demonstrates that at those points $N_{DoF} = m$.

Fig. 6(a) shows that those performance dips are completely removed if the Rx antennas are quadratically spaced (QLA). For distances above 93.75 m, the QLA achieves the same performance as the ULA. Using a QLA for both, Tx and Rx aperture, improves the performance for $R < 93.75$ m and enables the usage of single type of array for the entire deployment. Fig. 6(b) shows how the number N of antennas affects the performance. It is important to note that while N changes, the EIRP is kept constant. The curves show that for $N = 4$ the same minimum spectral efficiency is achieved as for $N = 8$, which is an opportunity to drastically reduce the cost of the fronthaul link.

B. ENHANCING LOS-MIMO WITH ANALOG MULTIPATH BEAMFORMING

Section III-A has shown that the number of DoF decreases as the distance between the Tx and Rx increases. This results in the performance drop due to the reduced channel rank, as observed in Fig. 4. To address this limitation and enhance LOS-MIMO systems, especially at larger distances, we propose an analog multipath beamforming scheme. This scheme allows us to leverage both the LOS and available NLOS path gains to increase the channel capacity. In contrast to conventional beamforming, where all antenna panels steer their beams into one direction, such as the LOS direction, the proposed analog multipath beamforming scheme adaptively points beams to multiple directions based on the strength of different channel paths and the array structure. This adaptive beamforming allows the system to take advantage of NLOS paths, which may arise due to ground reflections or the presence of purposely deployed Reflecting Intelligent Surfaces (RIS) or relays. This assumption of NLOS paths in a LOS connection is practical, especially when the Tx-Rx distance is large, and it helps to enhance the performance and capacity of the LOS-MIMO system.

In Fig. 7, popular array architectures are shown with three different mapping options from radio frequency (RF) chains to antenna panels, namely partial-connection (Fig. 7a), hybrid-connection (Fig. 7b), and full-connection (Fig. 7c). In the low complexity partial-connection, each RF chain is exclusively connected to a sub-section of the array. In the high complexity full-connection, each RF chain is mapped to all the antenna elements with a combiner adding up the weighted signals from all RF chains. We focus on the hybrid-connection with medium complexity, in which each RF chain is connected to a subset of panels (e.g., 2 panels), and each antenna panel is fed with weighted signals combined from a subset of RF chains (e.g., 2 chains), as shown in Fig. 7b. To implement this connection, we need to increase the number of antenna weights that are connected to each RF chain and a combiner for each element. In all architectures, the beams of the RF chains can be chosen independently. The advantage of this connection type is that RF power (in the case of Tx) can be moved between the beams of the same panel. If the beam of one direction requires less power, the amount of saved power can be given to another beam. Such a trade-off can be made based on the channel condition. This is in contrast to the partial-connection architecture where one cannot move RF power from the beam associated with RF-chain 1 to the beam for RF-chain 2. Next, we provide more details about the employed NLOS channel model, the precoder/beamforming design, and simulation results from the proposed analog multipath beamforming scheme.

1) NLOS CHANNEL MODEL AND ANALOG MULTIPATH BEAMFORMING

For the following we assume a system with parameters listed in Table 4. As mentioned in section above, we assume a carrier frequency $F_c = 80$ GHz and array apertures at Tx and Rx of $a_t = a_r = a = 1.68$ m. Since the separation between a Tx and Rx (i.e., R) does not exceed 500 m, this separation becomes less than the so-called Rayleigh distance, also known as the Fraunhofer distance [20]. In other words,

TABLE 4. Simulation parameters summary.

Parameter	Value	Parameter	Value
F_c	80GHz	Effective isotropic radiated power (EIRP) per panel	52.14dBm/ panel
Bandwidth (BW)	2.5GHz	Antenna element gain (AEG)	3 dB
a_t, a_r	1.68 m	Rain fade margin loss (RFM)	16 dB/Km
Panel	1×8	The path loss exponent (PLE)	2
Antenna per panel	8×16(128 elements)	Noise figure (NF)	9 dB
Panel separation	0.21 m	Thermal noise (TN)	-174dBm/Hz
R	10 to 500 m	Capacity gap margin (CGM)	5 dB
PA	7dBm		
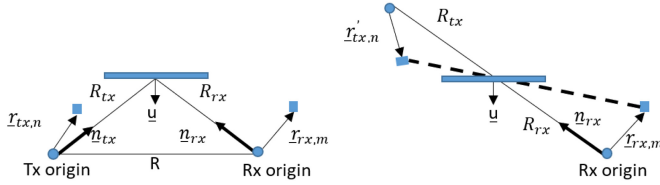
FIGURE 8. Near field NLOS channel model.

we have

$$R < R_{\text{rayleigh}} \approx \frac{2a^2}{\lambda} = 1505 \text{ m},$$

where λ is the wavelength. As a result, the farfield assumption is no longer valid. Thus, we cannot use the traditional channel models (e.g., the channel models proposed in 3GPP [21]) to model NLOS channel. In this case, we have to employ the nearfield assumption in modeling the NLOS channel. Towards that end, we adopt the channel model proposed in [22]. In this model, all reflectors are assumed to be limitless specular reflectors. For instance, if we have a transmit antenna n, a receive antenna m, and a reflector as shown in Fig. 8, then we compute the NLOS distance, $d_{NLOS}(x_m^r, x_n^t)$, by computing the LOS distance from the image of the transmit antenna behind the reflector and the receive antenna. This can be done by applying the following steps: Let $\underline{u}$ denote the unit vector perpendicular to the reflector plane. Moreover, let $\underline{n}_{tx}$ and R_{tx} represent the unit vector and the distance from the Tx origin to the reflection point, respectively. We also use $\underline{r}_{tx,n}$ to denote the vector from the Tx origin to the transmit antenna n. We similarly define $\underline{n}_{rx}$, R_{rx}, and $\underline{r}_{rx,m}$ for the receiver side. Note that, in modeling the NLOS channel, we suppose that the reflector positions are known. Hence, R_{tx}, and R_{rx} are known to us. To get the image of Tx antenna vector $\underline{r}_{tx,n}$ behind the reflector, we apply Householder transform [22] as follows

$$\underline{r}'_{tx,n} = \left(1 - 2\underline{u}\underline{u}^T\right)\underline{r}_{tx,n}, \quad (35)$$

where $\underline{r}'_{tx,n}$ is the image of the transmit vector $\underline{r}_{tx,n}$, and $\underline{u}^T$ is the transpose of vector $\underline{u}$. The NLOS distance $d_{NLOS}(x_m^r, x_n^t)$ is then computed as the distance between the image of the Tx antenna n and the Rx antenna m, which is given by

$$d_{NLOS}\left(x_m^r, x_n^t\right) = \left\|(R_{tx} + R_{rx})\underline{n}_{rx} + \underline{r}'_{tx,n} - \underline{r}_{rx,m}\right\|, \quad (36)$$

where $\|\cdot\|$ is the norm of a vector. The computed $d_{NLOS}(x^r, x^t)$ is hereafter used to construct the NLOS channel by substituting it into the following equation

$$H_{NLOS}(m, n) = g_{NLOS}e^{j\frac{2\pi}{\lambda}d_{NLOS}(x_m^r, x_n^t)}, \quad (37)$$

where H_{NLOS} is the channel matrix of the NLOS channel and g_{NLOS} denotes large-scale channel gain of NLOS paths. The overall channel is constructed by adding the LOS channel and the NLOS channel matrix as follows

$$H = \epsilon H_{LOS} + \sqrt{1 - \epsilon^2}H_{NLOS}, \quad (38)$$

where ϵ^2 represents the power percentage of the LOS path.

We now need to obtain the analog multipath beamforming weights such that both the LOS and NLOS paths are exploited. Therefore, our channel matrix H is represented by 3-dimensional matrix with size $N_{elem} \times N_{elem} \times (N_{tap} + 1)$, where N_{elem} is the total number of antenna elements at both Tx and Rx, and N_{tap} is number of channel taps that represent NLOS rays. It is also assumed that the entire array has $N_{elem} = 1024$ antenna elements (see also Table 4). As shown in Fig. 7(b), we employ the hybrid-connection in which each RF chain f_i is connected to two panels P_{i1} and P_{i2}, where i is the RF chain index. To derive the analog weights of each RF chain f_i, we consider the portion of the channel in frequency domain that is corresponding to panels P_{i1} and P_{i2} at Tx and Rx, denoted as $H_i(k)$, where k is the frequency index. Note that $H_i(k)$ is of size ($\frac{2N_{elem}}{N} \times \frac{2N_{elem}}{N} \times K$) for the considered hybrid structure, where N is the number of antenna panels and K the used FFT size for obtaining frequency domain channel. The number of antenna elements of each panel is $\frac{N_{elem}}{N} = 128$ (see Table 4). We then compute the wideband channel covariance in frequency domain, for the hybrid connection structure, as follows

$$\text{CovH}_i = \sum_{k=0}^{K-1} H_i^*(k) \times H_i(k), \quad (39)$$

where $H_i^*(k)$ is the Hermitian matrix of $H_i(k)$. We thereafter compute the two strongest eigen vectors, V_{i1} and V_{i2}, of the matrix CovH_i. These vectors, V_{i1} and V_{i2}, are of size ($\frac{2N_{elem}}{N} \times 1$) and represent the beams that point toward the directions carrying most of the channel power. These vectors construct the weights for RF chains. In particular, we assign V_{i1} to odd RF chains and V_{i2} to even ones. Fig. 9 illustrates

$$W_{\text{Analog}} = \begin{bmatrix} V_{11} & V_{22} & & & & & & 0 \\ & & V_{31} & V_{42} & & & & \\ & & & & V_{51} & V_{62} & & \\ 0 & & & & & & V_{71} & V_{82} \end{bmatrix} \quad (1024 \times 8)$$
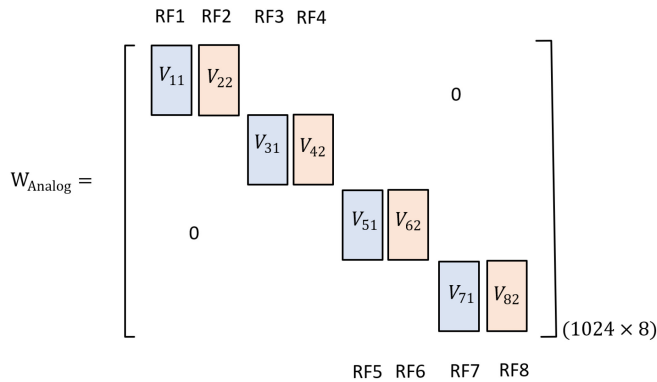
FIGURE 9. Precoder matrix structure in hybrid-connection case.

the construction of the (analog) precoder matrix. We assign different powers to different RF chains thereby satisfying the power constraint of each panel. These power values can be chosen proportional to the eigen values associated with the selected eigen vectors.

The above method is intended for the scenario when LOS-MIMO has a reduced DoF at large distances. However, when the LOS-MIMO operates at a shorter distance with sufficient DoF, the traditional partial-connection with constant phase offset (CPO) beams pointing towards LOS direction has a superior performance. It is worth noting that the hybrid-connection can always fall back to the partial-connection by assigning zeros to the first half of the weight vectors assigned to even RF chains and to second half of the weight vectors assigned to odd RF chains. That way we can assure a leading performance at all distances using the hybrid-connection compared to the partial-connection. In a prior study [23], it was demonstrated that a relay can establish a reliable NLOS path, thereby enhancing the channel capacity of a LOS-MIMO system. However, this approach comes with higher costs due to additional hardware, deployment, and power consumption. Our proposed solution aims to achieve similar goals while avoiding the additional costs.

2) SIMULATION RESULTS FOR ANALOG MULTIPATH BEAMFORMING

We present some simulation results to compare the performance of the hybrid-connection and partial-connection in presence of NLOS channel. We also investigate the performance of full-connection case, in which each panel is connected to all RF chains (see Fig. 7c). The precoder in full-connection case is constructed similarly to what we illustrated in Section III-B1 with two different steps: (a) Instead of considering a portion of channel matrix, we consider the whole matrix (i.e., we consider the channel H in frequency domain with size ($N_{elem} \times N_{elem} \times K$)). (b) instead of computing two strongest eigen vectors and assigning them alternatively to RF chains (as illustrated in Section III-B1), we compute the N strongest eigen vectors and assign each one of them to each RF chain. Therefore, the full-connection

acts as an upper bound for other connection types considered in this paper.

We now illustrate our simulation settings. The panel structure at Tx and Rx is ULA $N \times 1$ (i.e., we have $N = 8$ vertically aligned panels). Each panel is equipped with 16×8 antenna elements. The optimized separation between panels is 0.21 m, resulting in a vertical aperture size of 1.68 m of the array. The bandwidth is $BW = 2.5$ GHz. The radiated power of each antenna element is limited to $PA = 7$ dBm. Hence, the effective isotropic radiated power per panel is $EIRP = 52.14$ dBm/panel. The antenna element gain (AEG) is 3 dB. The path loss exponent (PLE) is 2. Rain fade margin loss (RFM), noise figure (NF), and thermal noise (TN) are 16 dB/Km, 9 dB, and -174 dBm/Hz, respectively. We consider 5 dB for Shannon capacity gap margin (CGM). All the above parameters are summarized in Table 4. The SNR for a link between a single Tx panel and a single Rx panel is then computed in dB as follows

$$SNR_{calc} = EIRP + 10\log_{10} 128 + AEG + 20\log_{10}\left(\frac{\lambda}{4\pi}\right)$$
$$- RFM \cdot \frac{R}{1000} + PLE \cdot 10\log_{10}\frac{1}{R} - CGM.$$

We also suppose the error vector magnitude (EVM) of the phase noise, I/Q imbalance, non-linearities, and so on is -30 dBc. Thus, the SNR is capped at 30 dB using the following equation:

$$\frac{1}{SNR} = EVM + \frac{1}{SNR_{calc}}, \quad (40)$$

where SNR_{calc} and EVM are in linear scale. Regarding the NLOS channel, we assume that the reflectors are distributed on a sphere around the Tx, where the sphere radius is $\frac{R}{2}$. We suppose that there is only one reflection on the sphere, after which the reflected rays reach out to the receiver. The reflectors' positions are determined using the angles of departure, where angles of departure values are taken from CDL-B channel model in 3GPP [21]. For simplicity and in keeping with the assumption of a specular reflection, we suppose that there is only one strong NLOS ray. Next, we present our simulation results.

Figs. 10 and 11 illustrate the achievable spectrum efficiency (SE) in bps/Hz versus Tx-Rx distance for ULA in the existence of weak and strong NLOS paths. The NLOS paths can come from either ground reflections or purposely deployed RIS. As observed in both figures, the full-connection architecture outperforms the other two architectures and acts as an upper bound. However, implementing the full-connection architecture is prohibitively costly. On the other hand, the hybrid-connection with multipath beamforming (BF) can provide a 10% to 30% SE gain compared to the partial-connection with LOS BF starting from $R = 200$ m, even for a relative weak NLOS channel with 10% power (i.e., when $\epsilon^2 = 0.9$). For a stronger NLOS channel with 40% power in Fig. 11, the hybrid-connection with multipath beamforming can provide up to 30% to 50% SE
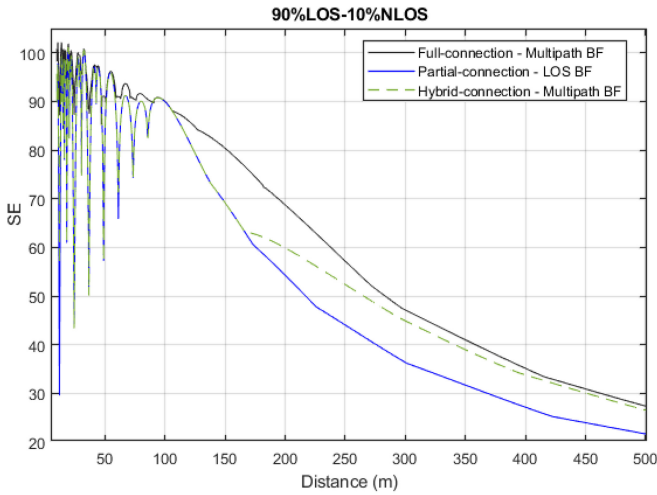
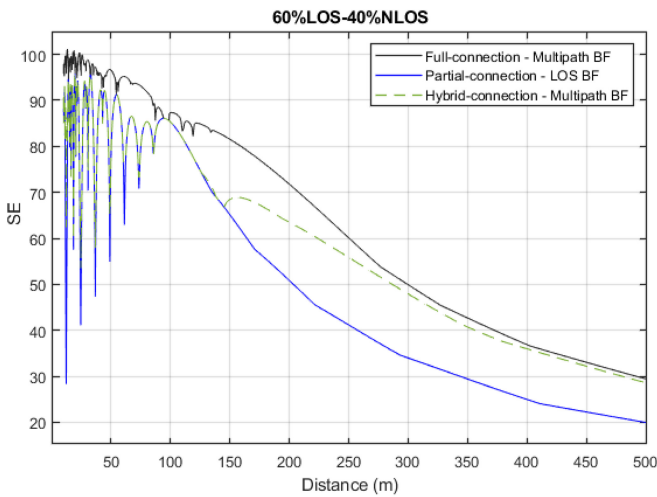**FIGURE 10.** SE vs. distance for ULA with weak NLOS.

FIGURE 11. SE vs. distance for ULA with strong NLOS.

gain compared to the partial-connection for large distances R > 250 m. This improvement comes from the fact both LOS and NLOS are exploited in the hybrid-connection with multipath beamforming, at the cost of moderately higher implementation complexity compared to the partial-connection. In the simulation, we assign the same power to all used layers and perform a rank adaptation in computing the capacity (i.e., we use minimum number of layers that provide us with maximum SE). We also assume minimum mean square error (MMSE) receiver. The beamforming matrixes for the full-connection and hybrid-connection are constructed in a way explained above, while the beamforming matrix of the partial-connection is constructed using CPO beams pointing towards LOS direction.

IV. SAMPLE-LEVEL OUTER CODE FOR ULTRA-RELIABLE WIRELESS FRONTHAULING

Along with robust performance and high spectral efficiency, which can be achieved via an optimized design of LOS-MIMO as discussed so far in this paper, the WFH must
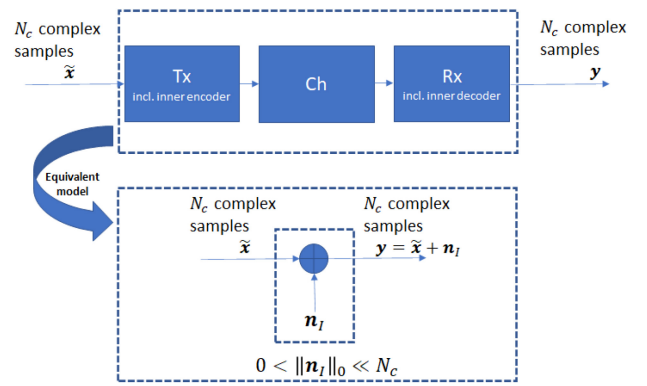

FIGURE 12. Fronthaul link model and abstraction.

also allow for improved communication reliability and comply with low latency requirements. The latter attributes can be typically obtained in a communication link by the introduction of an outer code, which assists in overcoming any inherent residual error floor stemming from the deficiencies of the inner code, for instance, low-density parity-check (LDPC) codes, especially when encoding relatively short to intermediate data and control blocks. This way an extended reliability can be met without the latency overhead involved in resorting to fronthaul retransmissions.

Now, having the fronthaul, by its modus operandi, conveying sample-level information, for instance I/Q, log-likelihood ratio (LLR) or constellation symbol samples, naturally incentivizes the design of a concatenated outer code, providing an additional layer for error detection and correction, which operates directly on the samples. The latter paradigm comes in contrast to the common practice of concatenating a conventional bit-level error-correcting codes as the Reed-Solomon or BCH codes, as applied for example in DVB-S2 [24]. Adopting such a sample-level coding allows also for an unequal bit protection in the sense that one can implicitly prioritize the correction of flips in the most significant bits (MSBs) over recovering from small perturbations in the least significant bits (LSBs). Thus, as shall be shown, the proposed fronthaul outer code facilitates detecting, and in certain cases also correcting, the more significant sample-level alterations while deemphasizing the effect of the weaker noise contaminations.

A. FRONTHAUL ABSTRACTION MODEL
Consider a fronthaul link model, as depicted in the upper pane of Fig. 12. The fronthaul transmission link consists of the three typical component blocks: transmitter (Tx), channel (Ch) and receiver (Rx). The transmitter and receiver are assumed to already encapsulate an inner encoder and decoder, respectively, to provide some channel error recovery. Let $\tilde{x} \in \mathbb{C}^{N_c}$ be an N_c-length sequence of complex samples transmitted through the fronthaul, while $y \in \mathbb{C}^{N_c}$ denotes the N_c-length sequence of complex samples reconstructed at the output of the inner decoder at the receiver.
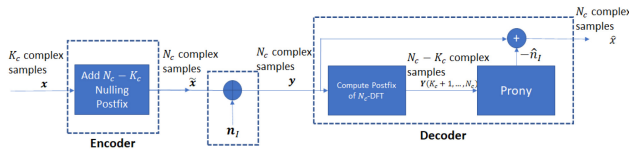
FIGURE 13. Proposed encoder and decoder.

An equivalent abstracted model to such a fronthaul system link would be as depicted in the lower pane of Fig. 12. According to such an abstraction, one may look at the input complex sequence $\tilde{x}$ as being altered by an N_c-length sparse impulse noise vector $\boldsymbol{n_I} \in \mathbb{C}^{N_c}$ to generate the recovered data vector $\boldsymbol{y}$. Again, the data samples sequence $\tilde{x}$ here could represent, for instance, I/Q samples, LLR samples or hard-decision constellation symbols, depending on the actual fronthaul split option being adopted and whether the model describes uplink or downlink transmission. Now, even under a powerful (inner) error-correcting code like a well-designed LDPC code, one may still have to deal with some residual errors or an error floor in the recovered vector **y** in the higher SNR regime.

Thus, achieving ultra-reliable communication requirements necessitates the removal of such an unavoidable sparse (i.e., the impulse noise vector's l_0-support, $\|n_I\|_0$, is substantially smaller than its length N_c) noise effect. One way of removing the post-inner code residual errors is via the mechanism of error detection and retransmission of data packets as being commonly done in wireless access, for example, by adding a cyclic redundancy check (CRC) and retransmitting post-LDPC faulty codeblocks. However, here within the fronthaul framework we would like to explore and leverage a different mechanism which possibly does not require retransmissions, thus also allows for further lowering the error floor but without incurring the latency toll.

B. SAMPLE-LEVEL ENCODER
In this work, we introduce a sample-level encoder, that operates directly on the complex-valued samples, rather than on their binary representation. The left (pre-channel) side of Fig. 13 presents a depiction of the encoder which adds an $(N_c - K_c)$-length nulling postfix to the original K_c-length sequence of samples. The nulling postfix is generated such that the DFT of the new extended N_c-length block of samples will yield the nulling of the last $(N_c - K_c)$ complex samples in the frequency domain.[1] The nulling postfix operation adheres to $\tilde{x}_i = x_i$ for $i = 1, \ldots, K_c$ and $\tilde{X}_i \triangleq DFT_{N_c}\{\tilde{x}\}_i = 0$ for $i = K_c + 1, \ldots, N_c$, where $\boldsymbol{x}$ and $\tilde{x}$ correspond to the outer encoder's input and output vectors, respectively. Note that appending the nulling postfix creates in effect a sample-level error-correcting code over the complex numbers with a

---

1. As a matter of fact, any function consisting of a sum of exponentials in time may be applied for the generation of the nulling postfix. To this end, we choose the DFT function due to its widespread use and computationally efficient implementation.

coding rate K_c/N_c, where the samples composing the nulling postfix serve as the code's redundancy, or parity, samples.

C. SAMPLE-LEVEL DECODER
The accompanying sample-level decoder is illustrated on the right (post-channel) side of Fig. 13. Per the N_c-length vector of received samples, $\boldsymbol{y}$, one computes the $(N_c - K_c)$-length postfix of the N_c-length DFT output, $\boldsymbol{Y}$, that is the last $(N_c - K_c)$ complex entries of the frequency-domain vector $\boldsymbol{Y}$. This $(N_c - K_c)$-length postfix is then fed into the *Prony Algorithm*, as described in the following, which in turn yields the estimate of the noise vector $\boldsymbol{n_I}$, thus can subsequently be negated from the received vector of the time-domain samples $\boldsymbol{y}$, and finally reconstruct the original vector of samples $\hat{\boldsymbol{x}}$.

The enabling claim (see [25]) of such a sample-level error-correcting code is that as long as the l_0-support of the noise vector is less or equal to half the length of the redundancy postfix (rounded to the nearest integer towards minus infinity), namely $\|n_I\|_0 \leq \lfloor \frac{N_c - K_c}{2} \rfloor$, then the detrimental effect of such a sparse residual impulse noise can be perfectly detected and eliminated from the received samples. To put differently, if although the inner code's protection the inner decoded sequence of complex samples, $\boldsymbol{y}$, still suffers from some alterations by a residual sparse noise, or in the case that effectively a few samples in $\boldsymbol{y}$ are being erased, then the outer code allows for recovery from up to $\lfloor \frac{N_c - K_c}{2} \rfloor$ such arbitrary errors within the N_c-length complex-valued codeword $\boldsymbol{y}$. Note that in the absence of ambient dense noise, like additive white Gaussian noise (AWGN), effecting all transmitted samples, or alternatively in the high SNR regime, the proposed outer code allows for perfectly overcoming $\lfloor \frac{N_c - K_c}{2} \rfloor$ errors, of any magnitude, within a block of N_c transmitted fronthaul samples. Now, even in a lower SNR regime, the outer code provides a mechanism for prioritizing the protection, detection, and recovery from (a few) intense errors, which may flip the MSBs, over mild to low intensity random errors, stemming from the ambient noise, which may mostly affect the LSBs. Another appealing attribute to the proposed coding scheme is its reliance, in both the encoder and decoder, on linear processing involving DFT and the solution of linear systems.

At the heart of the proposed sample-level coding mechanism lies a curve-fitting algorithm from the 18th century, known as Prony's method ([26] and Section IV-C1). Let $f(x)$ be an unknown function, with the side information about its composition of a sum of η complex exponentials. Thus, it is evident that the function $f(x)$ can be completely characterized by knowing (at least) 2η of its equally spaced samples. This observation is quite intuitive since there are exactly 2η degrees of freedom in specifying $f(x)$: η unknown complex amplitudes and η unknown exponents.

Now in the underlying communication problem, the exponential-sum function is taken to be the DFT and the number of unknown exponentials, η, is set to be equal to half of the length of the parity postfix, floored to the largest integer, $\lfloor \frac{N_c - K_c}{2} \rfloor$, which in turn corresponds in our model

and code design to the number of non-zero (or above some small threshold) entries of the latent noise vector, n_I. In other words, in light of the above curve-fitting observation, setting $\eta = \lfloor \frac{N_c - K_c}{2} \rfloor$, corresponding to η unknown error locations and η unknown error values, one needs to have at least $\nu \geq N_c - K_c$ samples of the noise's DFT to be able to completely specify the noise in the frequency domain (viz. $f(x)$).

We are ready now to connect this important observation from curve-fitting theory to the code design: at the encoder the DFT of $(N_c - K_c)$-length postfix of the transmitted codeword, $\widetilde{x}$, was intentionally nulled, hence the postfix for the DFT of the noise vector, n_I, will be identical, by design, to the postfix of the DFT of the received sample codeword, y. Now, this allows the reconstruction of the noise vector n_I by applying Prony's method. For completeness, in the following section the Prony algorithm is formally described in more detail.

1) THE PRONY ALGORITHM

Consider a latent continuous function of the form

$$f(x) = C_1 e^{\gamma_1 x} + C_2 e^{\gamma_2 x} + \cdots + C_\eta e^{\gamma_\eta x}, \quad (41)$$

where C_i and $\gamma_i (i = 1, \ldots, \eta)$ are η pairs of unknown complex pre-factor and exponent, respectively. Common examples for such a function, $f(x)$, are the DFT and inverse DFT. Now, further assume the function $f(x)$ is known only at $\nu \geq 2\eta$ equally spaced samples, that is, $f[l] = f(c + l\Delta)$, where $c \in \mathbb{R}$, $\Delta \in \mathbb{R}^+$ and $l = 0, \ldots, \nu - 1$. Within our problem formulation, the goal is to be able to perfectly reconstruct the 2η unknowns, C_i and γ_i, from the ν observed samples.

The solution to this essentially curve-fitting problem is provided by Prony's method [26]. First, define $\delta_i \triangleq e^{\gamma_i}$, thus one gets the following $\nu \times \eta$ linear system representation

$$f[i] = \sum_{j=1}^{\eta} C_j \delta_j^i, \quad i = 0, 1, 2, \ldots, \nu - 1. \quad (42)$$

Now, let assign the η-tuple $\{\delta_1, \delta_2, \ldots, \delta_\eta\}$ to be the roots of the polynomial equation

$$\delta^\eta - \alpha_1 \delta^{\eta-1} - \alpha_2 \delta^{\eta-2} - \cdots - \alpha_{\eta-1} \delta^1 - \alpha_\eta = 0, \quad (43)$$

and solve the following $(\nu - \eta) \times \eta$ linear system[2] for the coefficients α_i

$$\sum_{i=0}^{\eta-1} f[i+k]\alpha_{\eta-i} = f[\eta+k], \quad k = 0, 1, 2, \ldots, \nu - 1 - \eta. \quad (44)$$

Once the polynomial coefficients, α_i, are inferred from (44), then one can backtrack to recover the polynomial roots δ_i from (43), and consequently the complex pre-factors C_i can be also directly found from (42). To conclude, solving the set of equations (42)-(44) allows for completely specifying the sum of η exponentials composing the latent function $f(x)$ through observing as low as only 2η of its samples.

---

2. Note that since $\nu \geq 2\eta$ the composed linear system is guaranteed not to be underdetermined.

D. SAMPLE-LEVEL CODING EXAMPLE

For the sake of clarity and exposition, in this section an illustrative toy example for the end-to-end workings of the proposed outer coding is provided. In reference to the flow and notation in Fig. 13, consider a vector of $K_c = 6$ 64-QAM information symbols, $x = \{-3 + 7j, 7 + 3j, -7 - 3j, -5 + 7j, 1 + 7j, 3 + 3j\}^T$. Assuming a rate $3/4$ outer code, the sample-level codeword is of length $N_c = 8$, thus $N_c - K_c = 2$ nulling postfix parity samples are appended to x to yield $\widetilde{x}_i = \{x^T, -42.46 + 38.31j, -6.31 - 48.46j\}^T$, and to be transmitted through the equivalent channel.[3]

Now assume, for instance, that the residual noise vector, n_I, has only a single non-zero entry due to the error floor of the inner channel code, or alternatively owing to an erroneous slicing at the receiver, such that $n_I(3) = 2 + 2j$ (and n_I is zero elsewhere). Then, at the receiver, the 3rd sample within the $N_c = 8$-length sample-level codeword is being altered and corrupted from $\widetilde{x}(3) = -7 - 3j$ to $y(3) = -5 - 1j$. At the outer decoder on the receiver's side, we first compute the $N_c - K_c = 2$ postfix of an $N_c = 8$-DFT to yield the two samples $Y(7) = -2 - 2j$ and $Y(8) = -2 + 2j$, which are then fed into the Prony Algorithm (Section IV-C1). Since in this example the number of parity samples is $N_c - K_c = 2$, it means we are able to recover from a single $\lfloor \frac{N_c - K_c}{2} \rfloor = 1$ complex error in the received sequence y. In this example solving the Prony equations (42)-(44) yields the noise value of $\widehat{n}_I(i+1) = Y(7)^7 / Y(8)^6 = 2 + 2j$ (and $\widehat{n}_I$ is zero elsewhere), while the non-zero location is revealed to result in $i = -j8/(2\pi) \log(Y(7)/Y(8)) = 2$. Hence, we have completely specified and recovered the noise vector, thus able to subtract it from the received y vector, and successfully recover the original $K_c = 6$ 64-QAM information symbols, $x = \widehat{x}(1:6)$.

We have simulated this exact same example with $60,000$ information symbols, where within each of the $10,000$ generated codewords a single sample out of the $N_c = 8$ composing samples was randomly nulled, to get perfect decoding and an overall zero error in the recovered symbol sequence. Once $2 > \lfloor \frac{N_c - K_c}{2} \rfloor$ out of the 8 samples within the codeword are randomly nulled then the normalized mean-square-error of the decoded symbol sequence jumps, as expected, to 18 dB. Note the appealing property of the proposed decoder in inherently detecting its incapability in recovering from too many errors, that is, having to deal with more than $\lfloor \frac{N_c - K_c}{2} \rfloor$ sample alterations. Such a breakdown of the decoder can be identified by taking the formulation in Section IV-C1 for the particular case of using the DFT as the exponential-sum function $f(x)$, thus the indices of the error locations are intertwined with the inferred polynomial roots δ_i via

$$i = \text{Re}\left\{ j \frac{N_c}{2\pi} \log(\delta_i) \right\}, \quad (45)$$

---

3. For better peak-to-average power ratio (PAPR) considerations, note that one may also arbitrarily scale the postfix redundancy samples and descale them appropriately at the receiver side. In the subsequent link-level simulation results (Section IV-E) the nulling postfix parity samples are reciprocally scaled by a factor of the codeword length, N_c, to yield sample values within the range of the 64-QAM constellation grid.

TABLE 5. Link level simulation parameters for fronthaul and access links.

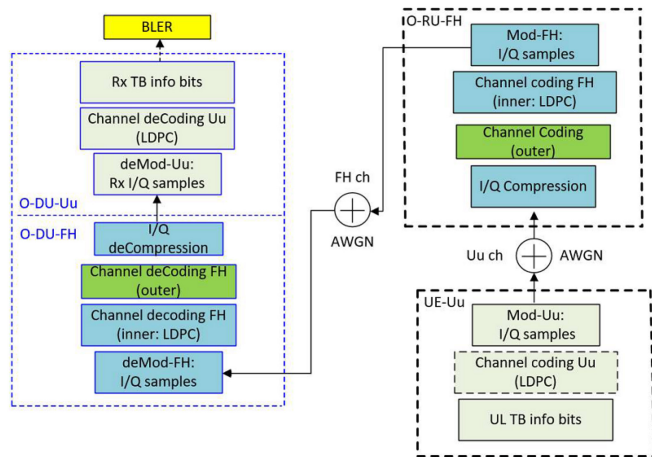|	Fronthaul	Access
Link level channel	AWGN	AWGN
MCS	index $= 23$: rate $= \frac{797}{1024}, 256 - \mathrm{QAM}$	index $= 23$: rate $= \frac{873}{1024}, 64 - \mathrm{QAM}$
SNR region [dB]	$[15.52, 26.09, 30.70] - ($ offset $= 1$ or $0.8)$	16.5 to 19
I/Q bit-width	9 bits (with block floating point compression [8])	16 bits (no compression)
Number of MIMO layers	3	1
Fronthaul outer coder $\left(\frac{K_c}{N_c}\right)$	$\frac{6}{8}$	N/A

FIGURE 14. Simulated link-level block diagram for access and fronthaul (FH) links in the uplink.
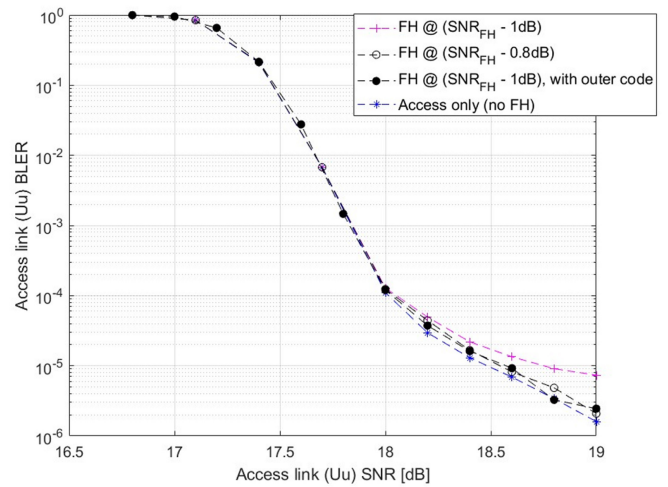

FIGURE 15. BLER performance of access link with WFH.

where $\mathrm{Re}\{\cdot\}$ denotes taking the argument's real value. Hence whenever the outer decoder computes noninteger error indices in (45), it is deemed non-constructive, and its output can be easily bypassed and ignored. In the next section the proposed outer coding scheme is evaluated in a more realistic end-to-end fronthaul setup in which in addition to the detrimental sparse impulse error $\boldsymbol{n}_I$, surviving the inner coding, all samples also undergo contamination with some operational AWGN.

E. LINK LEVEL SIMULATION RESULTS

In this section we evaluate the end-to-end block error rate (BLER) performance for a 5G Uu access uplink concatenated with a WFH. Fig. 14 shows the link-level block diagram of the baseband processing for the simulated end-to-end uplink. The source bits at a UE are first LDPC coded and modulated before being transmitted through the Uu access link channel. The signal is then received at the O-RU and processed with I/Q compression,[4] optionally applying I/Q

sample-level outer coding,[5] the inner fronthaul LDPC channel encoding and modulation, before being conveyed through the WFH using an OFDM waveform (with 1024 subcarriers, out of which 768 are of data, and 11 symbols per slot). On the O-DU side, the wireless fronthaul module reverses the processing done at the O-RU and feeds the baseband I/Q to the regular O-DU unit for the UE's bits recovery. We simulate a case with the WFH Tx-Rx largest supported distance at R = 500 m and assuming the WFH-DU (Rx) antenna has a 30-degree offset from the WFH-RU (Tx) antenna boresight direction. This represents the worst-case scenario for the proposed fronthaul design. In a pure LOS-MIMO channel with the designed antenna configuration and link budget parameters, as given in Table 4, the WFH link generates a 3-layer MIMO channel with a resulted $\mathrm{SNR_{FH}} = [15.52, 26.09, 30.70]$ dB, respectively. The link-level simulation is conducted with the above per-layer SNR for the fronthaul link and for a range of SNR values for the Uu access link, under an AWGN channel for both. More simulation parameters are listed in Table 5.

Fig. 15 shows the perceived BLER of the end-to-end Uu access uplink, including the concatenated WFH segment (as depicted in Fig. 14), as a function of the access link SNR.

---

4. O-RAN's block-floating point (BFP) procedure [8] is implemented for the I/Q compression in which a physical resource block (PRB) of data (12 subcarriers with 16-bit uncompressed I and Q samples) is compressed to a bit-signed mantissa (of 9-bit I and 9-bit Q) for each sub-carrier and a common unsigned scaling exponent is shared across the entire compression block (viz. PRB).

5. In the results, whenever the sample-level outer concatenated code is used then the preceding I/Q compression step is applied on the data samples, while the parity samples are uniformly quantized with 16-bit similarly to the Uu access I/Q samples.

The access only BLER blue curve ("*") refers to the case of a limitless, or genie, fronthaul (viz. assuming no fronthaul segment needed at all to connect the UE to the network), hence this curve serves essentially as a lower bound and as the best Uu BLER performance one can hope for in the simulated configuration (approaching a BLER level of down to the order of 10^{-6}). For all other three curves simulated, the fronthaul is set at a pre-designed SNR_{FH} working point which turns out to be more than sufficient for the chosen modulation and coding scheme (MCS) for the fronthaul. Thus, the pre-designed SNR is adjusted and degraded (by either 1 or 0.8 dB) so that the fronthaul can operate at a target BLER region of 10^{-5}. Such an SNR backoff could be also realized as an SNR margin reserved for the detriments of any practical implementations. As shown by the curve in magenta ("+") for the simulated concatenated access and fronthaul link (flow as in Fig. 14 and parameters taken from Table 5, without applying the outer code), with an SNR offset of 1 dB, the overall Uu BLER is floored to around 10^{-5}. To allow the Uu to experience and deliver lower BLER, the wireless fronthaul could be engineered, via a lower fronthaul SNR offset of 0.8 dB (black curve with empty circles "○"), again without applying any outer coding, to be almost non-discernable from the access link's BLER performance in the perfect fronthaul case (namely, the blue curve of ("*")).

Alternatively, as illustrated by the black curve with the full circles ("●"), another means to reapproach the 'ideal' fronthaul BLER performance and lowering back the BLER to the order of 10^{-6} is by keeping the original, more power-efficient, lower fronthaul SNR level of $[15.52 \ 26.09 \ 30.70] - 1$ dB, yet enabling the sample-level outer coder. Thus, it may be observed that incorporating the outer code within the fronthaul transceiver assists in correcting some of (both the Uu's and fronthaul's) inner codes' residual error and subsequently improve the overall perceived access link BLER performance. To put differently, in the simulated configuration the proposed sample-level outer code exhibits an effective coding gain of around $1 - 0.8 = 0.2$ dB.

Note in passing that in some cases of high enough SNR, or low enough BLER, further power-boosting, or even taking a lower code rate, for the inner (LDPC) code will only have a diminishing returns effect or will encounter a practically unavoidable fixed error floor. These are exactly the cases where the proposed sample-level outer code, being very natural to the fronthaul configuration, becomes very useful.

V. CONCLUSION AND FUTURE WORKS

In this work, we have proposed a range of enabling technologies for WFH that offer significant improvements in performance and cost-efficiency. Our investigations in LOS-MIMO systems demonstrate the robustness of linear array configurations against misalignments caused by various factors, making them a reliable and viable solution. The introduction of a novel non-uniform linear array design, based on quadratic spacing of antenna elements,

has effectively addressed the performance dips observed in traditional uniform linear arrays for short link distances. Moreover, our exploration of harvesting specular reflections from buildings, ground, and RIS in combination with LOS has shown substantial performance gains for long link distances. The hybrid-connection array architecture with multipath beamforming proves to be a promising solution for achieving enhanced system capacity and coverage. Furthermore, A novel sample-level coding scheme for wireless fronthaul deployment allows lowering the error floor beyond the one achieved by LDPC codes. Simulation of the end-to-end fronthaul uplink with only 9-bit block-floating point compression, based on SO 7-2x, has shown that the proposed sample-level coding approaches the access link error performance, which would be experienced by the user with an 'ideal' fronthaul. In conclusion, our research has shown that wireless fronthaul is a promising transport technology, particularly in scenarios where fiber connections are not feasible or economically viable. The technologies introduced in this paper offer practical and effective solutions to improve the efficiency, reliability, and cost-effectiveness of wireless fronthaul systems.

In our forthcoming work, we plan to expand our research along the following directions:

- Network Densification: As the network becomes denser, the possibility of multiple RUs being served by multiple CUs and DUs arises. The efficient coordination and communication among multiple DUs and RUs will be investigated, considering aspects such as network channel state information (CSI) feedback, centralized scheduling, and potential trade-offs and limitations in practical deployments.
- Application of Reconfigurable Intelligent Surfaces: RIS and meta-surfaces have emerged as potential candidates for 6G networks. The hardware implementation of RIS relies on the concept of programmable meta-surfaces. To harness its full potential, we aim to develop novel modeling and designs for applying RIS assisted LOS-MIMO in WFH systems.
- Enabling Cell-free Massive MIMO: These systems offer substantial data rate and coverage gains, but typically rely on fiber-based fronthaul for communication between the central processing unit and distributed access points (APs). The feasibility of using wireless fronthaul in cell-free massive MIMO systems will be examined, aiming to meet high data rate demands while reducing infrastructure costs and enhancing deployment flexibility and adaptability in such systems.

REFERENCES

[1] V. M. Nguyen and M. Kountouris, "Performance limits of network densification," *IEEE J. Sel. Areas Commun.*, vol. 35, no. 6, pp. 1294–1308, Jun. 2017.
[2] P. H. Kuo and A. Mourad, "Millimeter wave for 5G mobile fronthaul and backhaul," in *Proc. Eur. Conf. Netw. Commun. (EuCNC)*, Oulu, Finland, Jun. 2017, pp. 1–5.

[3] K. Zaman and M. M. Mowla, "A millimeter wave fronthauling solution for open RAN paradigm in 5G and beyond networks," in *Proc. IEEE Int. Conf. Telecommun. Photon. (ICTP)*, Dhaka, Bangladesh, Dec. 2021, pp. 1–5.

[4] S. Hur, T. Kim, D. J. Love, J. V. Krogmeier, T. A. Thomas, and A. Ghosh, "Millimeter wave beamforming for wireless backhaul and access in small cell networks," *IEEE Trans. Commun.*, vol. 61, no. 10, pp. 4391–4403, Oct. 2013.

[5] C. Saha and H. S. Dhillon, "Millimeter wave integrated access and backhaul in 5G: Performance analysis and design insights," *IEEE J. Sel. Areas Commun.* vol. 37, no. 12, pp. 2669–2684, Dec. 2019.

[6] M. Jiang et al., "Wireless fronthaul for 5G and future radio access networks: Challenges and enabling technologies," *IEEE Wireless Commun.*, vol. 29, no. 2, pp. 108–114, Apr. 2022.

[7] "Study on new radio access technology: Radio access architecture and interfaces," 3GPP, Sophia Antipolis, France, Rep. TR 38.801, V14.0.0, Apr. 2017.

[8] "O-RAN alliance specifications: O-RAN fronthaul control, user and synchronization plane specification," O-RAN Fronthaul Working Group, O-RAN Alliance e.V., Alfter, Germany, Mar. 2020.

[9] R. I. Rony, E. Lopez-Aguilera, and E. Garcia-Villegas, "Cost analysis of 5G fronthaul networks through functional splits at the PHY layer in a capacity and cost limited scenario," *IEEE Access*, vol. 9, pp. 8733–8750, 2021.

[10] J. K. Chaudhary, J. Bartelt, and G. Fettweis, "Statistical multiplexing in fronthaul-constrained massive MIMO," in *Proc. Eur. Conf. Netw. Commun. (EuCNC)*, Oulu, Finland, Jun. 2017, pp. 1–5.

[11] L. Zheng and D. N. C. Tse, "Diversity and multiplexing: A fundamental tradeoff in multiple-antenna channels," *IEEE Trans. Inf. Theory*, vol. 49, no. 5, pp. 1073–1096, May 2003.

[12] F. Bohagen, P. Orten, and G. E. Oien, "Design of optimal high-rank line-of-sight MIMO channels," *IEEE Trans. Wireless Commun.*, vol. 6, no. 4, pp. 1420–1425, Apr. 2007.

[13] S. Saab, D. Kim, S. Abu-Surra, G. Xu, and J. Zhang, "Path towards Tbps communications: LoS MIMO theory, simulation and measurement analysis," in *Proc. IEEE Globecom Workshops (GC Wkshps)*, Rio de Janeiro, Brazil, Dec. 2022, pp. 1796–1801.

[14] F. Sohrabi and W. Yu, "Hybrid analog and digital beamforming for mmWave OFDM large-scale antenna arrays," *IEEE J. Sel. Areas Commun.*, vol. 35, no. 7, pp. 1432–1443, Jul. 2017.

[15] A. Pizzo and A. Lozano, "On Landau's eigenvalue theorem for line-of-sight MIMO channels," *IEEE Wireless Commun. Lett.*, vol. 11, no. 12, pp. 2565–2569, Dec. 2022.

[16] S. J. Orfanidis (Rutgers Univ., Piscataway, NJ, USA). *Electromagnetic Waves and Antennas*. (2016). [Online]. Available: http://www.ece.rutgers.edu/ orfanidi/ewa/

[17] H. J. Landau and H. Widom, "Eigenvalue distribution of time and frequency limiting," *J. Math. Anal. Appl.*, vol. 77, no. 2, pp. 469–481, 1980.

[18] D. Slepian and H. O. Pollak, "Prolate spheroidal wave functions, fourier analysis and uncertainty—I," *Bell Syst. Tech. J.*, vol. 40, no. 1, pp. 43–63, Jan. 1961.

[19] H. Do, N. Lee, and A. Lozano, "Reconfigurable ULAs for line-of-sight MIMO transmission," *IEEE Trans. Wireless Commun.*, vol. 20, no. 5, pp. 2933–2947, May 2021.

[20] K. T. Selvan and R. Janaswamy, "Fraunhofer and Fresnel distances: Unified derivation for aperture antennas," *IEEE Antennas Propag. Mag.*, vol. 59, no. 4, pp. 12–15, Aug. 2017.

[21] "Study on channel model for frequencies from 0.5 to 100 GHz," 3GPP, Sophia Antipolis, France, Rep. 38.901, V16.1.0, Jan. 2020.

[22] Y. Hu, M. Yin, S. Rangan, and M. Mezzavilla, "Parametrization of high-rank line-of-sight MIMO channels with reflected paths," in *Proc. IEEE 23rd Int. Workshop Signal Process. Adv. Wireless Commun. (SPAWC)*, Dresden, Germany, 2022, pp. 1–5.

[23] B. T. Walkenhorst and M. A. Ingram, "Repeater-assisted capacity enhancement (RACE) for MIMO links in a line-of-sight environment," in *Proc. IEEE Int. Conf. Commun. (ICC)*, Oulu, Finland, Aug. 2009, pp. 1–6.

[24] *Digital Video Broadcasting (DVB); Second Generation Framing Structure, Channel Coding and Modulation Systems for Broadcasting, Interactive Services, News Gathering and Other Broadband Satellite Applications (DVB-S2)*, ETSI Standard EN 302 307-1, V1.4.1, Nov. 2014.

[25] J. Wolf, "Redundancy, the discrete fourier transform, and impulse noise cancellation," *IEEE Trans. Commun.*, vol. 31, no. 3, pp. 458–461, Mar. 1983.

[26] R. Prony, F. M. Gaspard, and R. De Baron, "Essai exprimental et analytique: Annuaire de l'École polytechnique," *J. Lécole Polytechnique Paris*, vol. 1, no. 22, pp. 24–76, 1795.

JUERGEN CEZANNE (Senior Member, IEEE) received the Dipl.-Ing. and Dr-Ing. degrees in electrical engineering from Technical University Darmstadt in 1986 and 1991, respectively. He is currently a Senior Director of Technology with Qualcomm, leading PHY/MAC layer research efforts for 5G NR mmWave systems. Before Qualcomm, he was with Flarion Technologies developing and implementing solutions for FlashOFDM. Prior to that, he was a Distinguished Member of Technical Staff with Bell Labs, Lucent Technologies. His current research interests include phased arrays, beam management, hybrid beamforming, and MU-MIMO.
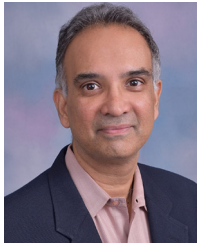
MEILONG JIANG (Senior Member, IEEE) received the Ph.D. degree in electrical engineering from The University of Hong Kong in 2006. He was a Postdoctoral Researcher with Columbia University in 2008. He is currently a Senior Staff Engineer with Qualcomm Technologies Inc., NJ, USA, where his work focuses on mmWave, massive MIMO, MU-MIMO, and active antenna system technology enhancements for 5G and beyond.
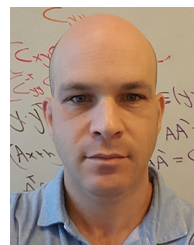
ORI SHENTAL (Senior Member, IEEE) received the B.Sc. and Ph.D. degrees in electrical engineering from Tel-Aviv University, Israel, in 1996 and 2006, respectively. He is with Qualcomm. He is also an Adjunct Associate Professor with Columbia University. He was a Postdoctoral Researcher with the University of California, San Diego, from 2006 to 2008. His fields of research are wireless communications, information theory, signal processing, probabilistic inference, and machine learning. He had received several awards for academic and research and development excellence.

AHMED M. BEDEWY received the B.S. and M.S. degrees in electrical and electronics engineering from Alexandria University, Egypt, in 2011 and 2015, respectively, and the Ph.D. degree in electrical and computer engineering from The Ohio State University in 2021. He currently works as a Senior Engineer with Qualcomm Flarion Technologies. He received the Awarded Certificate of Merit and First-Class Honors from the Electrical and Electronics Engineering Department from 2006 to 2011. His article received the Runner-Up for the Best Paper Award at ACM MobiHoc 2020.

ASHWIN SAMPATH (Senior Member, IEEE) received the Ph.D. degree in electrical engineering from Rutgers University. He is a Senior Director of Technology with Qualcomm, leading millimeter-wave deployment-related research topics. Prior to Qualcomm, he was with Texas Instruments from 2003 to 2005, and before that he was a Distinguished Member of Technical Staff with Bell Labs, Lucent Technologies from 1997 to 2003. He has 25 years of industry experience in wireless technology research, standardization, and product development.

JUNYI LI (Fellow, IEEE) is the Vice President of Engineering with Qualcomm, responsible for research and development systems in the New Jersey office. Prior to that, he was a Co-Founder of Flarion Technologies and a Key Inventor with Flash-OFDM. He holds over 800 U.S. patents. He is a coauthor of *OFDMA Mobile Broadband Communications* (Cambridge University Press).

OZGE KOYMEN (Member, IEEE) received the B.S. degree in electrical and computer engineering from Carnegie Mellon University in 1996, and the M.S. and Ph.D. degrees in electrical engineering from Stanford University in 1997 and 2003, respectively. He is a Senior Director of Technology with Qualcomm, where he has been since 2006. He has led the 5G/6G Millimeter-Wave Program with Qualcomm Technologies since early 2015, from early conceptual evaluation to commercial deployment. His previous areas as a Technical Contributor include wireless backhaul, small cells, LTE-D, LTE, and UMB.